

FULL PAPER

Open Access

Climatology of the diurnal tides from eCMAM30 (1979 to 2010) and its comparison with SABER

Quan Gan^{1,4*}, Jian Du¹, William E Ward², Stephen R Beagley³, Victor I Fomichev³ and Shaodong Zhang⁴

Abstract

The extended Canadian Middle Atmosphere Model (eCMAM) was recently run in a nudged mode using reanalysis data from the ground to 1 hPa for the period of January 1979 to June 2010 (hence the name eCMAM30). In this paper, eCMAM30 temperature is used to examine the background mean temperature, the spectrum of the diurnal tides, and the climatology of the migrating diurnal tide Dw1 and three nonmigrating diurnal tides De3, Dw2, and Ds0 in the stratosphere, mesosphere, and lower thermosphere. The model results are then compared to the diurnal tidal climatology derived from Sounding of the Atmosphere using Broadband Emission Radiometry (SABER) observations between 40 to 110 km and 50° S to 50° N from January 2002 to December 2013. The model reproduces the latitudinal background mean temperature gradients well except that the cold mesopause temperature in eCMAM30 is 10 to 20 K colder than SABER. The diurnal tidal spectra and their relative strengths compare very well between eCMAM30 and SABER. The altitude-latitude structures for the four diurnal tidal components (Dw1, De3, Dw2, and Ds0) from the two datasets are also in very good agreement even for structures in the stratosphere with a weaker amplitude. The largest discrepancy between the model and SABER is associated with the seasonal variation of De3. In addition to the Northern Hemisphere (NH) summer maximum, a secondary maximum occurs during NH winter (December-February) in the model but is absent in SABER. The seasonal variations of the other three diurnal tidal components are in good agreement. Interannual time series of Dw1 and De3 from both eCMAM30 and SABER reveal variability with a period of 25 to 26 months, which indicates the modulation of the diurnal tides by the stratospheric quasi-biennial oscillation (QBO).

Keywords: Diurnal tides; Migrating; Nonmigrating; eCMAM30; SABER; QBO

Background

Atmospheric solar tides are planetary-scale waves with periods that are harmonics of a solar day (i.e., 24, 12, 8 h, etc.). Solar tides can be detected in basic atmosphere parameters such as temperature, wind, and density or in tidally induced effect such as chemical composition and airglow emissions. Tides can be generated by either the diabatic heating of the atmosphere (Chapman and Lindzen 1970) or wave-wave interactions (Teitelbaum and Vial 1991; McLandress and Ward 1994; Angelats I Coll and Forbes 2002). The diabatic heating source includes direct absorption of solar radiation (for example, infrared radiation by water vapor in the troposphere, ultraviolet radiation by ozone in the stratosphere, and extreme

ultraviolet radiation by molecular oxygen in the thermosphere) and tropospheric latent heat release due to deep convection in the tropics (Hagan 1996; Hagan and Forbes 2002). Solar tides with a specific period can be further divided into two subgroups: (1) migrating tides which propagate westwards with phase velocity following the apparent motion of the Sun and (2) nonmigrating tides which have different phase velocities to the migrating tides and can propagate westwards, eastwards, or remain stationary relative to the ground.

Except for occasional extreme planetary wave activity, atmospheric solar tides represent the dominant dynamical component of the mesosphere and lower thermosphere (MLT) region (Forbes 1982). Tides that propagate into the MLT region reach large amplitudes and profoundly affect the large-scale dynamics, chemistry, and energetics of this region. They transport momentum and energy upward from the source regions (primarily the troposphere and

* Correspondence: quan.gan@louisville.edu

¹Department of Physics and Astronomy, University of Louisville, Louisville, KY 40292, USA

⁴School of Electronic Information, Wuhan University, Wuhan, China
Full list of author information is available at the end of the article

stratosphere) and then dissipate in the MLT region through various instabilities, molecular viscosity, ion drag, and wave-wave or wave-mean flow interactions (Forbes et al. 1993; Miyahara et al. 1993). Tides can modify the upward propagation of gravity waves and their momentum deposition in the MLT region via critical layer filtering mechanisms (Fritts and Vincent 1987) and via modulation of the buoyancy frequency (Preusse et al. 2001). They also play a major role in the diurnal cycle of chemically active species and large-scale constituent transport in the MLT region (Coll and Forbes 1998; Ward 1998; Ward et al. 1999; Marsh and Russell 2000; Zhang et al. 2001) and thus influence the chemical heating in this region (Smith et al. 2003). Tides can also cause the mesospheric inversion layers (MIL) at low latitude (Gan et al. 2012). In addition, atmospheric tides have recently been found to cause significant spatial and temporal variability in the ionosphere (Forbes et al. 2000; England 2012 and references within).

In the present study, we focus on the diurnal component of the solar tides (i.e., the diurnal tides). The sun-synchronous or migrating diurnal tide $Dw1^a$ is arguably the largest and most persistent feature of the large-scale wind and temperature fields in the equatorial and low-latitude MLT region (Mukhtarov et al. 2009). However, the nonmigrating diurnal tidal amplitudes have been found to be equal to or exceed the migrating diurnal tidal amplitude at some locations and/or time (Lieberman 1991; Forbes et al. 2001, 2003a, b; Oberheide and Gusev 2002; Du 2008; Ward et al. 2010) and cause significant longitudinal variability in the MLT (Ward et al. 2010) and ionospheric region (England 2012). The climatology of both migrating and nonmigrating diurnal tides has been revealed by satellite temperature/wind observations such as the High Resolution Doppler Interferometer (HRDI)/Wind Imaging Interferometer (WINDII)/Microwave Limb Sounder (MLS) on board the Upper Atmosphere Research Satellite (UARS) (Hays and Wu 1994; McLandress et al. 1996; Khattatov et al. 1996; Talaat and Lieberman 1999; Ward et al. 1999; Forbes et al. 2003a, b; Manson et al. 2004; Huang and Reber 2004; Forbes and Wu 2006), the TIMED Doppler Interferometer (TIDI)/Sounding of the Atmosphere using Broadband Emission Radiometry (SABER) on board the Thermosphere Ionosphere Mesosphere Energetics and Dynamics (TIMED) satellite (Wu et al. 2006; Forbes et al. 2006; Zhang et al. 2006; Oberheide et al. 2006; Wu et al. 2008a, b; Pancheva et al. 2009; Xu et al. 2009b; Sakazaki et al. 2012) in the MLT region, and the CHALLENGING Minisatellite Payload (CHAMP) radio occultation (RO) (Zeng et al. 2008; Pirscher et al. 2010; Xie et al. 2010) in the upper troposphere and lower stratosphere (UTLS) region. Ground-based instruments such as radars and lidars have also been used routinely for diurnal tide observations

in the range of 80 and 120 km (Fritts and Isler 1994; Vincent et al. 1988, 1998; Yi 2001; Manson et al. 2002; She et al. 2004; Zhang et al. 2004; Yuan et al. 2006, 2008; Lu et al. 2012; Huang et al. 2012, 2013a, b; Gong et al. 2013).

Besides observations, models including sophisticated general circulation models (GCMs) and simpler mechanistic models are used to simulate the latitudinal structure and seasonal variability of the diurnal tides (Forbes 1982; Miyahara and Miyoshi 1997; Miyahara et al. 1999; Hagan et al. 1995, 2009; McLandress 1997, 2002a; Hagan and Roble 2001; Grieger et al. 2002; Huang et al. 2005, 2007; Mayr et al. 2005; Ward et al. 2005; Du 2008; Chang et al. 2012; Huang et al. 2013a, b). Although the general characteristics of the diurnal tides can be understood from classical tidal theory (Chapman and Lindzen 1970), detailed modeling studies are important. They provide the means to examine the tidal structure cleanly (observations are generally affected by sampling issues) and help in the interpretation of the observed features through investigation of physical mechanisms such as tidal forcing, tidal propagation and dissipation, and tide-mean flow and tide-wave interactions.

Although ground-based instruments can provide long-term and high-spatial-and-temporal-resolution observations, they can only be deployed at a limited number of locations. As a result, they cannot provide a globally tidal climatology. In addition, ground-based observations from a single station cannot resolve tidal components with different zonal wave numbers. Satellite measurements of atmospheric tidal parameters have the advantage of including data points from many geographic locations. However, the high orbital inclination needed to get nearly global coverage also results in a slow local time precession rate, which introduces sampling and aliasing errors. These issues are particularly troublesome when trying to resolve atmospheric structures that are ordered in local time and are nonsteady. The time interval required to sample observations covering 24 h of local time is long enough for the dynamic structures to vary significantly in form. This makes resolving any short-term variability in dynamic features difficult when using satellite observations alone (Forbes et al. 1997). The development of numerical models and their comparison with observations are vitally important for testing our understanding of the atmospheric systems. If all of the relevant physical processes are correctly represented, the model should provide a faithful simulation of atmospheric tides and support the interpretation of observed tidal features. Deficiencies in the model simulations indicate that important processes have been omitted or inadequately treated.

While free-running models are important for understanding the mechanisms responsible for the observed tidal features, they cannot be used to simulate specific tidal events observed in the real atmosphere. Specific

comparisons can, however, be made if the troposphere and stratosphere are constrained by the observations, as is done with data assimilation systems. The global meteorological analysis (operational)/reanalysis data have been widely used for meteorological and climatological studies from the troposphere to the stratosphere over the last decade. The main advantage of these datasets is that various operational observations from the surface to the stratosphere (approximately 50 km) are assimilated into self-consistent first-principle models, leading to uniformly gridded and globally available data for many variables. To date, no middle atmosphere model is data-assimilated for the whole domain due to the scarceness of observations in the MLT region. However, there has been effort on using assimilated meteorological analysis data to constrain the middle atmosphere model in the troposphere and stratosphere (Marsh 2011; McLandress et al. 2013; Davis et al. 2013).

The extended Canadian Middle Atmosphere Model (eCMAM) (Fomichev et al. 2002; Beagley et al. 2010) is recently nudged to interim version of the European Center for Medium-Range Weather Forecasts Reanalysis (ERA Interim; Dee et al. 2011) data up to 1 hPa using a simple relaxation procedure from January 1979 to June 2010 (hence the name eCMAM30). Diurnal tides from ERA Interim have shown the most similar results to those from SABER in the stratosphere comparing to other well-known reanalysis datasets (Sakazaki et al. 2012). Herein, we describe the background temperature field and the diurnal tides from eCMAM30 in the stratosphere and MLT region and validate our simulations against temperature derived from SABER/TIMED. Note that SABER data are not assimilated in ERA Interim reanalysis, making it feasible to evaluate the nudged eCMAM30 data. From this study, we are able to make quantitative statements for the first time on how well the eCMAM is simulating the diurnal tides comparing to real-time observations.

In this paper, we focus on the climatology of the background temperature field and the diurnal tidal components from eCMAM30 and the extent to which they match the equivalent parameter obtained using SABER observations. The term climatology refers to multiyear averages and their seasonal variations. The climatology is useful for predicting general conditions to be seen at a particular location and time of year. The tidal fields to be described are a function of altitude, latitude, zonal wave number, and month. Therefore, it is only possible to illustrate a small fraction of our results in this paper. The authors can provide additional figures that depict the full range of our results upon request.

The paper is organized as follows. In 'Data and methods', we describe the two datasets used. This includes a very brief discussion of the SABER data and a more detailed

discussion of the eCMAM30 simulation. In 'Results and discussion', we present the results, starting with the climatology of eCMAM30 background temperature and its comparison with SABER. We then present the diurnal tidal spectrum as a function of wave number (from -5 to $+5$: the wave numbers identify tidal 'components' or 'tides', and positive (negative) zonal wave numbers imply westward (eastward) propagation) from both eCMAM30 and SABER. This is followed by the climatological altitudinal-latitudinal structures of the migrating diurnal tide Dw1 and three nonmigrating diurnal tides De3, Dw2, and Ds0 from both datasets. A description of the seasonal variability of these four diurnal tidal components is also presented. We end this section with a simple discussion and comparison of the interannual variability of the diurnal tides (e.g., Dw1 and De3) between eCMAM30 and SABER. Our main results are summarized in 'Conclusions'.

Data and methods

SABER observations

The SABER instrument was launched onboard the TIMED satellite on December 7, 2001. SABER is a ten-channel broadband radiometer covering a spectral range from 1.27 to 17 μm . The temperature profile is retrieved from two 15- μm and one 4.3- μm CO₂ radiometer channel measurements in the tangent height range spanning approximately 20 to 120 km. The local-thermodynamic-equilibrium (LTE) and non-LTE retrieval algorithms are used, respectively, at altitudes below 70 km and in the upper MLT region (Mertens et al. 2004). Remsberg et al. (2008) assessed the quality of version 1.07 temperature data and suggested that the random error is no more than 2 K below 70 km, while in the upper MLT region, the error increases with altitude from 1.8 K at 80 km to 6.7 K at 100 km. Yue et al. (2013) and Jiang et al. (2014) examined how the systematic and random errors in SABER temperature data may affect the calculation of the amplitudes of the migrating terdiurnal tide and 9-/13.5-day oscillations, respectively. They replaced the actual data by random noise in a normal distribution with the width of the measurement uncertainties and then performed Monte Carlo simulation. Their results show that the measurement uncertainties cause negligible errors in deriving the wave amplitudes and phases even at 120 km where the random error is as large as 10 K. The effective vertical resolution of SABER temperature is approximate 2 km. SABER is in a slow-processing polar sun-synchronous orbit and can only make measurements at two local times per day. The local time does shift a small amount each day (12 min), accumulating to 24 h for about 60 days at low to middle latitudes when both ascending and descending samples are combined. Due to the vertical sightline to the velocity of SABER, the

latitude coverage is from 53° latitude in one hemisphere to 83° in the other. We analyzed both SABER version 1.07 and the latest version 2.0 temperature data from January 2002 to December 2013 for this paper, and the difference between the two is minor. In this paper, only version 2.0 SABER temperature analyses are presented (see Huang et al. 2006; Xu et al. 2007a, b, and Smith 2012 for climatological temperatures using earlier versions of the SABER data).

SABER temperature data is analyzed as follows to extract the diurnal tides. Firstly, the data between January 2002 and December 2013 are sorted into latitude bins, which are 5° wide with centers offset by 2.5° (equator, 5° S/N, 10° S/N, 15° S/N... 50° S/N) from 50° S to 50° N. All the original profiles are interpolated to 1-km vertical spacing from 20 to 110 km before further analysis. Secondly, we calculate the zonal mean temperature profiles at each day using ascending and descending nodes, respectively. Least squares harmonic fitting is then performed on the daily zonal mean temperature profiles in the local time frame to extract the migrating tides at each altitude and latitude. The fitting equation includes four cosine terms corresponding to the migrating tides with the periods of 24, 12, 8, and 6 h and a constant term. To ensure nearly full 24-h local time coverage, the fittings are implemented in a 60-day running window with 1-day increment. Before each fitting, the daily zonal mean temperature is de-trended to minimize the aliasing of seasonal variation in background temperature on the migrating tide. The fitting equation at each altitude and latitude in local time frame is as follows:

$$\bar{T}_{\text{ZD}}(t_{\text{LT}}, z, \varphi) = \bar{T}_0 + \sum_{n=1}^4 A_n \cos(n\omega_0(t_{\text{LT}} - t_n)) \quad (1)$$

where \bar{T}_{ZD} is the daily zonal temperature, \bar{T}_0 is the 60-day averaged zonal mean temperature of both ascending and descending nodes, and A_n and t_n are the daily amplitude and phase of the migrating tides. t_n is defined as the local time when tides reach the maximum amplitude ($\omega_0 = \frac{2\pi(\text{radian})}{24(\text{hour})}$, t_{LT} is in hours, $n = 1$ to 4).

For the nonmigrating tides, the daily zonal mean temperature profiles are subtracted from original profiles at each day to obtain the residual temperature profiles. The same 60-day temporal window is utilized but in universal time frame to extract the daily amplitudes and phase of the nonmigrating diurnal tides from the residual profiles. The fitting equation also contains the stationary planetary waves with the zonal wave numbers 1, 2, and 3. The fitting equation at each altitude and latitude in universal time frame is as follows:

$$T_r(t_{\text{UT}}, \lambda, z, \varphi) = \overline{T_{r0}} + at_{\text{UT}} + \sum_{s=-5}^5 A_{1,s} \cos(\omega_0(t_{\text{UT}} - t_{1,s}) + s\lambda) + \sum_{k=1}^3 B_k \cos(k\lambda + \zeta_k) \quad (2)$$

where T_r is the residual temperature; $\overline{T_{r0}}$ is the 60-day averaged zonal mean residual temperature; at_{UT} denotes the linear trend; $A_{1,s}$ and $t_{1,s}$ are the amplitude and phase of diurnal nonmigrating tides with specified zonal wave number (s), respectively; $t_{1,s}$ is defined as the time when the nonmigrating tides reach the maximum at $\lambda = 0$; B_k and ζ_k are the amplitude and phase of stationary planetary wave with zonal wave number k ($\omega_0 = \frac{2\pi(\text{radian})}{1(\text{day})}$, t_{UT} is in days; λ is in radians; $s = -5, -4, -3, -2, -1, 0, 1, 2, 3, 4, 5$; and $k = 1$ to 3

eCMAM30 simulations

For this analysis, we have used the eCMAM (Beagley et al. 2000, 2010; Fomichev et al. 2002; McLandress et al. 2006) with a top at 2×10^{-7} hPa (geopotential height approximately 220 km but dependent on the solar cycle) that was enhanced by inclusion of neutral and ion chemistry. The model has a triangular spectral truncation of T32, corresponding to a 6° horizontal grid. There are 87 levels in the vertical, with a resolution varying from several tens of meters in the lower troposphere to approximately 2.5 km in the mesosphere. The previous version of the model included the non-LTE parameterization for the 15- μm CO₂ band; solar heating due to absorption by O₂ in the Schumann-Runge bands (SRB) and continuum (SRC) and by O₂, N₂, and O in the extreme ultraviolet spectral region; parameterized chemical heating; molecular diffusion and viscosity; and ion drag. The current version of the eCMAM also includes comprehensive stratospheric chemistry (de Grandpre et al. 2000) with radiatively interactive O₃ and H₂O, a simplified ion chemistry scheme (Beagley et al. 2007) over a vertically limited domain, and non-LTE treatment of the near-infrared CO₂ heating (Ogibalov and Fomichev 2003). The Hines (1997a, b) nonorographic GWD scheme is used in this model. The model includes realistic tidal forcing due to radiative heating, convective processes, and latent heat release (Scinocca and McFarlane 2004). These processes have been shown to provide the forcing necessary to generate the migrating and nonmigrating tides in the free-running eCMAM (McLandress 1998, 2002a, b; Ward et al. 2005; Du et al. 2007; Du and Ward 2010; Du et al. 2014).

Recently, the horizontal winds and temperature below 1 hPa from this version of the eCMAM are nudged (i.e., relaxed) to the 6 hourly horizontal winds and temperature from the ERA Interim reanalysis data from January 1979

to June 2010. The nudging approach is designated to primarily constrain synoptic space and times scales in the model, which are well represented in the reanalysis data. This is accomplished by performing the relaxation in spectral space and applying it only to horizontal scales with $n \leq T21$, where n is the total wave number. The nudging tendency has the form $-(X - X_R)/\tau_0$, where $\tau_0 = 24$ h is the relaxational timescale and X and X_R are, respectively, the model and reanalysis spectral vorticity, divergence, or temperature coefficients (Kharin and Scinocca 2012). Linear interpolation is used to compute the reanalysis variables at intermediate times between adjacent 6-h intervals (McLandress et al. 2013). No nudging of chemistry fields is included in eCMAM30.

Global total temperature is extracted from the model every 6 h for the period of January 1979 to June 2010. In order to obtain the background mean temperature and the monthly mean amplitude and phase of the diurnal tides (from zonal wave number -5 to $+5$), a 2-D Fourier transform in longitude and time is applied to the total temperature to get the spectrum density in the domain of wave frequency and zonal wave number. On the basis of the spectrum density corresponding to a particular tidal component, an inverse Fourier transform is used to derive its monthly mean amplitude and phase.

To facilitate the comparison between eCMAM and SABER, the results are interpolated with a 5-km vertical interval from 20 to 110 km for both datasets. The latitude range is from -87.5° N to 87.5° S for eCMAM30 and from 83° N (50° N) to 83° S (50° S) for SABER for the background mean (diurnal tidal amplitudes and phases) temperature comparisons. Monthly climatological background mean temperature and the amplitude and phase of the diurnal tides are calculated by vector averaging between January 1979 and June 2010 for eCMAM30 and between January 2002 and December 2013 for SABER. The above calculations are repeated for the overlapped period (January 2002 to June 2010) between eCMAM30 and SABER, and the difference is minor from the climatology calculated from each available period (not shown).

Results and discussion

Climatology of background temperature

The first step in the model validation is a comparison of the simulated zonal mean background temperature with the observations. Figure 1 shows the seasonally averaged zonal mean temperature in Northern Hemisphere (NH) spring (March, April, and May), summer (June, July, and August), autumn (September, October, and November), and winter (December, January, and February) obtained from eCMAM30 (left panel) and SABER (right panel). As can be seen from the comparisons for different seasons, there is very good agreement between the two datasets throughout the whole vertical domain

of 20 to 110 km. The model reproduces the latitudinal temperature gradients quite well: a cold winter lower stratosphere, an elevated winter stratopause, a warm summer stratopause, and a cold summer mesopause. Temperature increases rapidly in the thermosphere. The main differences between the model and the observations are that the cold mesopause in the model is about 10 to 20 K colder and the elevated stratopause is at a slightly higher altitude than the observations. The mesopause low temperature is a result of the balance between the weak absorption of solar energy by O_2 and the efficient radiation to space by CO_2 . Another source of global heating and cooling in the mesopause region is due to dissipating gravity waves and their interaction with the background atmosphere (Smith 2012). Middle atmosphere GCMs have been notorious for their inability to simulate the cold summer mesopause - the so-called 'cold pole problem'. A cold pole implies too little dynamical heating induced by angular momentum deposition from small-scale internal gravity waves (Shepherd 2000). Correct representation of gravity waves in GCMs still remains as a challenge issue.

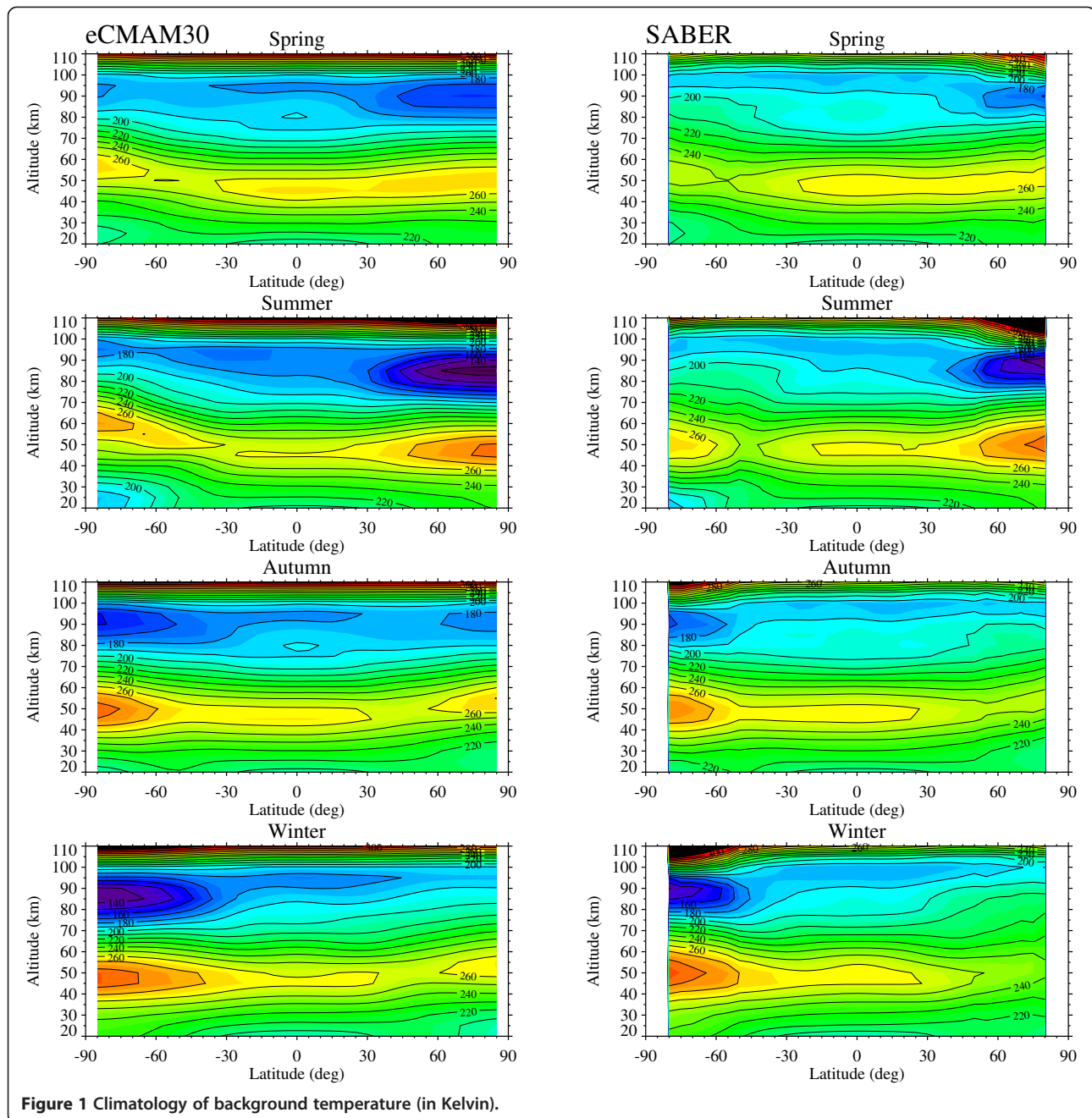
Another discrepancy between the model and SABER is that the increasing rate of temperature in the thermosphere (close to the upper limit of SABER's capability) is greater in the model than that in the SABER observations. However, both the model and SABER show a stronger vertical gradient in the summer hemisphere, which is again related to the dynamical summer (pole) to winter (pole) circulation and the resulting adiabatic heating/cooling effect (Smith et al. 2011). The SABER background temperatures shown here are consistent with previous SABER analyses such as Smith (2012). Overall, the zonal mean background temperature climatology is in very good agreement between eCMAM30 and SABER.

Diurnal tides

In this section, we provide the climatology of the diurnal tides (Dw1, De3, Dw2, and Ds0) for temperature from eCMAM30 (including their latitudinal-altitudinal structures and seasonal variations) and its comparison with SABER tidal observations. At the end of the section, a brief description of the interannual variability of the diurnal tides (Dw1 and De3) from eCMAM30 is presented and compared to SABER. The detailed discussion of the interannual variability is out of the scope of this paper and will be pursued in the future.

Spectral overview of the diurnal tides

For this paper, 11 components of the diurnal tide were analyzed (from wave number $s = -5$ to $+5$). Figure 2 depicts the normalized amplitude of the 11 diurnal tidal components at four altitudes as a function of latitude for NH spring (a) and summer (b). The tidal amplitude is



normalized to the maximum tidal amplitude to establish the relative significance of these oscillations at a particular altitude. And negative (positive) wavenumber denotes eastward (westward) propagation tidal component. The four altitudes (45, 60, 95, and 105 km) are chosen to represent the stratopause, lower mesosphere, mesopause, and lower thermosphere regions, respectively. The features at NH autumn (winter) are very similar to those at NH spring (summer); therefore, the figures are not shown. As illustrated in Figure 2, 11 diurnal tidal components are included in the spectrum, but in practice, relatively

few tidal components (such as Dw1, De3, Dw2, and Ds0) are found to dominate. These diurnal tidal components have also been identified in previous analyses of satellite and model data (Talaat and Lieberman 1999; Forbes et al. 2003a, b; Forbes and Wu 2006; Forbes et al. 2006; Zhang et al. 2006; Huang and Reber 2004; Manson et al. 2004; Du 2008; Du et al. 2014) and are now well-accepted diurnal tides of importance in the MLT region.

For the NH spring (March-May) at 45 km (Figure 2A), Dw1 is the dominant diurnal tidal component with a maximum located symmetrically at 15° to 85° and centered

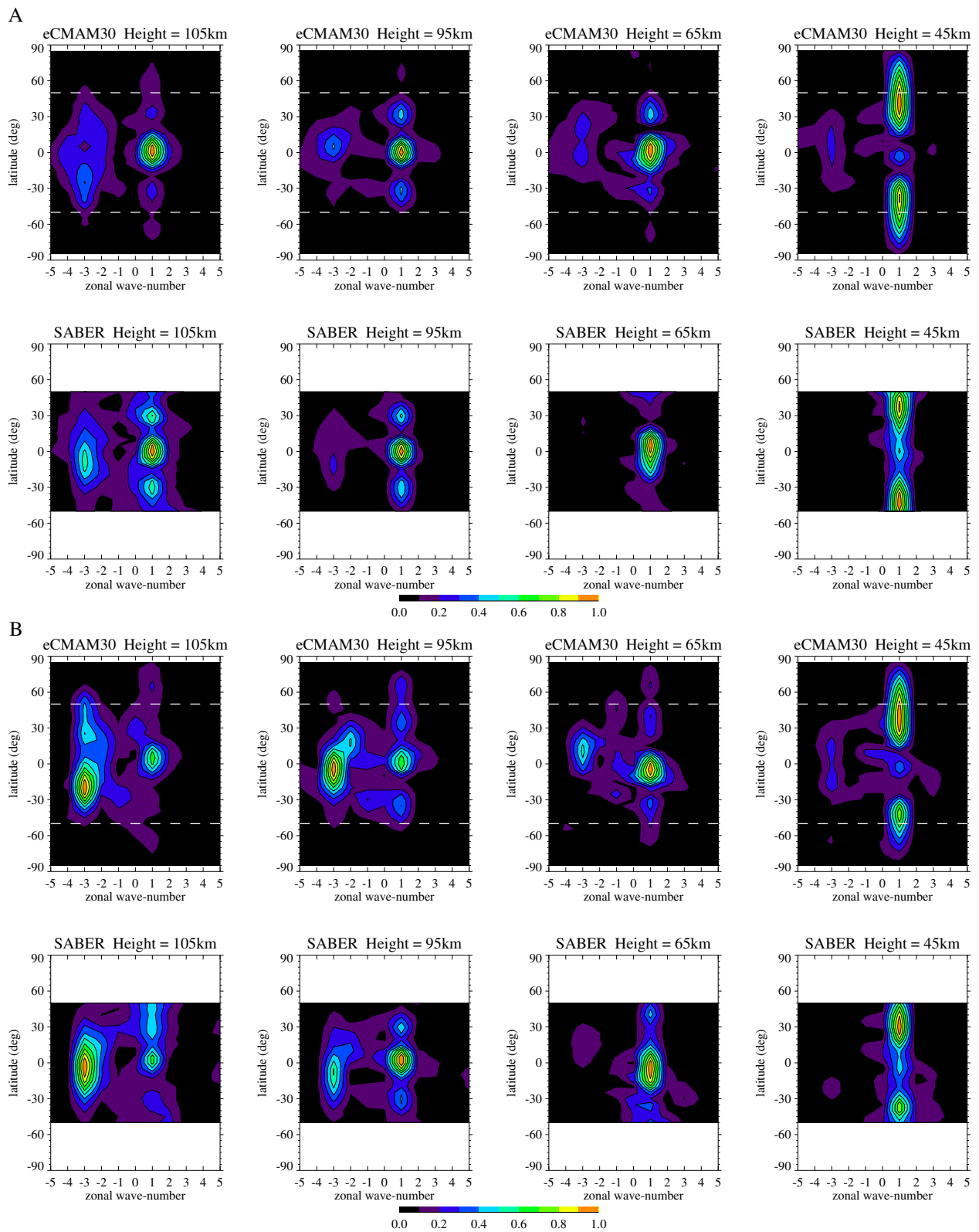


Figure 2 Normalized wavenumber spectra of the diurnal tides (from De5 to Dw5) at 45, 65, 95 and 105 km during NH spring (A) and summer (B) from eCMAM30 (upper panel) and SABER observation (lower panel). Positive (negative) wavenumber denotes westward (eastward) propagating tidal component. The latitude range for SABER is 50°N-50°S. White dashed lines denote 50°N/S. The contour scale is from zero to unity with the interval of 0.1.

at 40° to 50° of each hemisphere in the eCMAM30. There is a secondary maximum (20% to 30% of the primary maximum amplitude) located between 0° and 10° S. SABER also shows that Dw1 is the dominant component at this altitude, and its latitudinal structure compares very well with eCMAM30. The spectrum composition is richer in eCMAM30 than SABER at this latitude. Besides Dw1, De3 is present in the range of 30° S to 30° N with 20% of the maximum amplitude of Dw1 in eCMAM30. Other nonmigrating diurnal tidal components such as Ds0, De1, and De4 are also present with 10% of the maximum amplitude of Dw1. In SABER, the amplitude of De3 is smaller than 10% of that of Dw1 and therefore not shown in the figure. Ds0 and Dw2 are also present at a limited latitudinal range with amplitude of 10% of the maximum amplitude of Dw1.

At 65 km in the spring, the dominant component is still Dw1 in both eCMAM30 and SABER. However, its primary and secondary maxima are reversed from their counterparts at 45 km. The primary maximum of Dw1 is now located at the equatorial region in both eCMAM30 and SABER. Its secondary maximum is located symmetrically at 20° to 50° and centered at approximately 30° of each hemisphere in eCMAM30. The position of this secondary maximum in SABER is more pole-ward than eCMAM30 but is difficult to locate due to the cutoff latitude at 50° in SABER. De3 is present with 20% of the maximum amplitude of Dw1 in eCMAM30, but is still absent in SABER at this altitude. eCMAM30 still presents a richer spectrum than SABER. Besides Dw1 and De3, the nonmigrating tides Dw2, Ds0, De1, De2, De4, and De5 are also present with 10% of the maximum amplitude of Dw1 in eCMAM30. SABER only shows Ds0 and Dw2 in the spectrum at this altitude with relative amplitude of 10%.

At mesopause region (95 km) in the spring, the dominant diurnal tidal components are Dw1 and De3 for both eCMAM30 and SABER. The latitudinal structure of Dw1 is very similar to that at 65 km in both eCMAM30 and SABER and compares well between the two datasets. The latitudinal structures of De3 are consistent between eCMAM30 and SABER as well. However, the relative amplitude of De3 is different: it increases to 40% comparing to the maximum amplitude of Dw1 in eCMAM30 and only 20% in SABER. Besides Dw1 and De3, both eCMAM30 and SABER show the presence of Ds0, De1, and De2 at this altitude with 10% relative amplitude. eCMAM30 also shows the presence of Dw2, De4, and De5 with 10% relative amplitude.

At 105 km in the spring, the dominant components are still Dw1 and De3 for both eCMAM30 and SABER. As the overall latitudinal structures of Dw1 and De3 are similar, there are a few differences between the model and observations. The relative amplitude of the secondary

maximum for Dw1 decreases from 40% at 95 km to 20% at 105 km in eCMAM30, while it increases from 40% to 60% in SABER. The relative amplitude of De3 stays similar (40%) from 95 to 105 km with maximum location shifting from 10° N to 30° S. On the other hand, SABER observation shows that the relative amplitude of De3 increases from 20% at 95 km to 60% at 105 km and maximizes at the equatorial region (5° N to 20° S) at both 95 and 105 km. This hemispheric asymmetry associated with De3 has been reported by previous SABER analyses (Forbes et al. 2006; Zhang et al. 2006). Besides Dw1 and De3, both eCMAM30 and SABER show the presence of Dw2, Ds0, De2, De4, and De5 with relative amplitude of 10% to 20%. SABER also shows the presence of Dw3 and De1 at this altitude with relative amplitude of 10%.

During the NH summer (June-August) (Figure 2B), Dw1 and De3 are still the dominant diurnal tidal components for both eCMAM30 and SABER at all selected altitudes. However, their latitudinal structures and relative amplitudes are quite different from those of NH spring (Figure 2A). At 45 km, Dw1 is still characterized by broad mid- and high-latitude maxima in each hemisphere and a secondary maximum at the equator. However, the mid- and high-latitude maxima in the NH are much stronger than their counterparts in the Southern Hemisphere (SH), which results in hemispheric asymmetry. The above features for Dw1 are evident in both eCMAM30 and SABER. Similar to the NH spring, De3 is present at 45 km as 20% of the maximum Dw1 amplitude in eCMAM30 but is relatively absent in SABER. Both eCMAM30 and SABER show the presence of Ds0, Dw2, Dw3, and De1 with relative amplitude of 10% of the Dw1 maximum amplitude.

At 65 km in the summer, both eCMAM30 and SABER show the magnifying of the equatorial maximum and decreasing of the mid- and high-latitude maxima. The mid- and high-latitude maxima are 30% to 40% of the equatorial maximum in both eCMAM30 and SABER. SABER shows more hemispheric asymmetry between the two mid- and high-latitude maxima than eCMAM30. The relative amplitude of De3 reaches 50% of the maximum amplitude of Dw1 at this altitude in eCMAM30 although it is much smaller (10%) in SABER. Other nonmigrating tides such as Dw2, Dw3, Ds0, and De1 are also present in the spectrum for both eCMAM30 and SABER with relative amplitude of 10%.

The most dominant diurnal tidal component is De3 in eCMAM30 at 95 km during the NH summer. The relative amplitude of Dw1 is only 50% of the maximum amplitude of De3. SABER still shows Dw1 as the most dominant component with De3 being half of the maximum amplitude of Dw1 at this altitude. The overall spectrum agrees very well between eCMAM30 and SABER: the dominated diurnal components, the latitudinal structures of Dw1 and De3, and the slightly hemispheric asymmetry of the

secondary maximum associated with Dw1. Besides Dw1 and De3, De2 is also present in both eCMAM30 and SABER with relative amplitude of 30% to 40% of the maximum tidal amplitude. Other nonmigrating tides such as Dw2, Dw3, Ds0, and De1 are also present in the spectrum for both eCMAM30 and SABER with relative amplitude of 10%.

At 105 km in the summer, both eCMAM30 and SABER agree that De3 is the most dominant diurnal component. The latitudinal structure of De3 in eCMAM30 is slightly different from that in SABER: eCMAM30 shows one maximum located at 0° to 50° S and centered on 20° S and a secondary maximum (half of the primary maximum) located at 10° to 60° N and centered on 25° N, while SABER shows one broad maximum between 50° N and 50° S and centered on the equator. The maximum relative amplitude of Dw1 is 50% to 60% of that of De3 in eCMAM30 and located in the equatorial region. The secondary maxima at the mid- and high latitudes seen at 95 km are absent at this altitude in eCMAM30. In SABER, the maximum amplitude of Dw1 is about half of that of De3. The maxima are located at the equator and 10° to 30° N, respectively. This strong hemispheric asymmetry is not present in eCMAM30. Besides Dw1 and De3, there are other nonmigrating diurnal tidal components present in the spectrum such as Dw2, Ds0, De1, and De2 with 10% relative amplitudes in both eCMAM30 and SABER.

Overall, the tidal component composition and their relative strength at various altitudes compare very well between eCMAM30 and SABER. During the NH spring, the migrating Dw1 component has the largest monthly mean amplitude while the nonmigrating De3 component has the second largest monthly mean amplitude at all four altitudes. During the NH summer, the migrating Dw1 component has the largest monthly mean amplitude below 65 km while the nonmigrating De3 component becomes the strongest in the upper MLT region although the model and SABER disagree on the exact changeover altitude. The spectrum is richer in NH summer than NH spring due to the weaker amplitude of Dw1. The latitudinal structures of the diurnal tides between the model and SABER are also in very good agreement especially during NH spring. Besides Dw1 and De3, both the model and SABER show that Ds0 and Dw2 can be important at a certain season and altitude.

Altitude-latitude structures of the diurnal tides

In this section, we present the climatological altitude-latitude structures of the migrating component Dw1 and three nonmigrating components De3, Dw2, and Ds0 from both eCMAM30 and SABER. As shown in the previous section, Dw1 and De3 are the two most dominant diurnal tidal components from the troposphere to the MLT region. Dw2 and Ds0 are also persistently present in the

spectrum at various altitudes and seasons and believed to be generated by the nonlinear interaction between the migrating diurnal tide Dw1 and the stationary planetary wave with wave number 1 - SPW1 (Hagan and Roble 2001; Lieberman et al. 2004; Grieger et al. 2004). The altitude range presented in this section is from 40 to 110 km because the tidal perturbations below 40 km are small.

Figure 3 shows the cross section of the temperature amplitude (in Kelvin) and phase (in hour) of Dw1 as a function of latitude and altitude for March (a) and July (b) derived from eCMAM30 (left) and SABER (right). The months of March and July are chosen since Dw1 tends to maximize during equinox and minimize during solstice (more on seasonal variation in 'Seasonal variations of the diurnal tides'). For March (Figure 3A), both eCMAM30 and SABER show that the structure of Dw1 above 60 km is characterized with an equatorial maximum and two secondary maxima located symmetrically in the mid-latitudes (near $\pm 35^\circ$) of each hemisphere. Dw1 in this region is mainly excited by H₂O solar radiation absorption in the troposphere, but tropospheric latent heating (Forbes et al. 1997) and ozone absorption (Hagan 1996) can also make nonnegligible contributions. The equatorial maximum is located between 100 and 110 km in eCMAM30 with maximum amplitude of 28 to 30 K. The same maximum in SABER is located lower than that in eCMAM30 at 95 to 100 km with lesser maximum amplitude of 20 K. Wave growth with height over the equator is more rapid for eCMAM30 than SABER above 60 km, which suggests that the eCMAM may be under-damping the wave (i.e., not enough eddy diffusivity). The secondary maxima in the mid-latitudes have similar maximum amplitude of 8 to 9 K in both eCMAM30 and SABER.

The phase structure is symmetric over the equator and in very good agreement between the model and SABER. Both SABER and eCMAM30 show the 180° phase shift between the equatorial and mid-latitude maxima. The phase decreases with height, which indicates the upward propagation of the tide Dw1 in this region. The vertical wavelength of the propagating tide is about 20 to 25 km in both eCMAM30 and SABER, which is also in agreement with previous SABER (Zhang et al. 2006; Forbes et al. 2006; Smith 2012) and MLS analyses (Forbes and Wu 2006). Significant amplitudes (2 to 4 K) also exist at high latitudes (60° to 70°) in eCMAM30, indicating the presence of trapped modes, possibly indicative of an in situ source of excitation (i.e., chemical heating).

Between 40 and 60 km in March (Figure 3A), the latitudinal structure of Dw1 is different from above and is characterized by two maxima located in the mid- and high latitude of each hemisphere. These features are in good agreement between the model and SABER observations with monthly mean amplitude of 2 to 4 K. The SH maxima

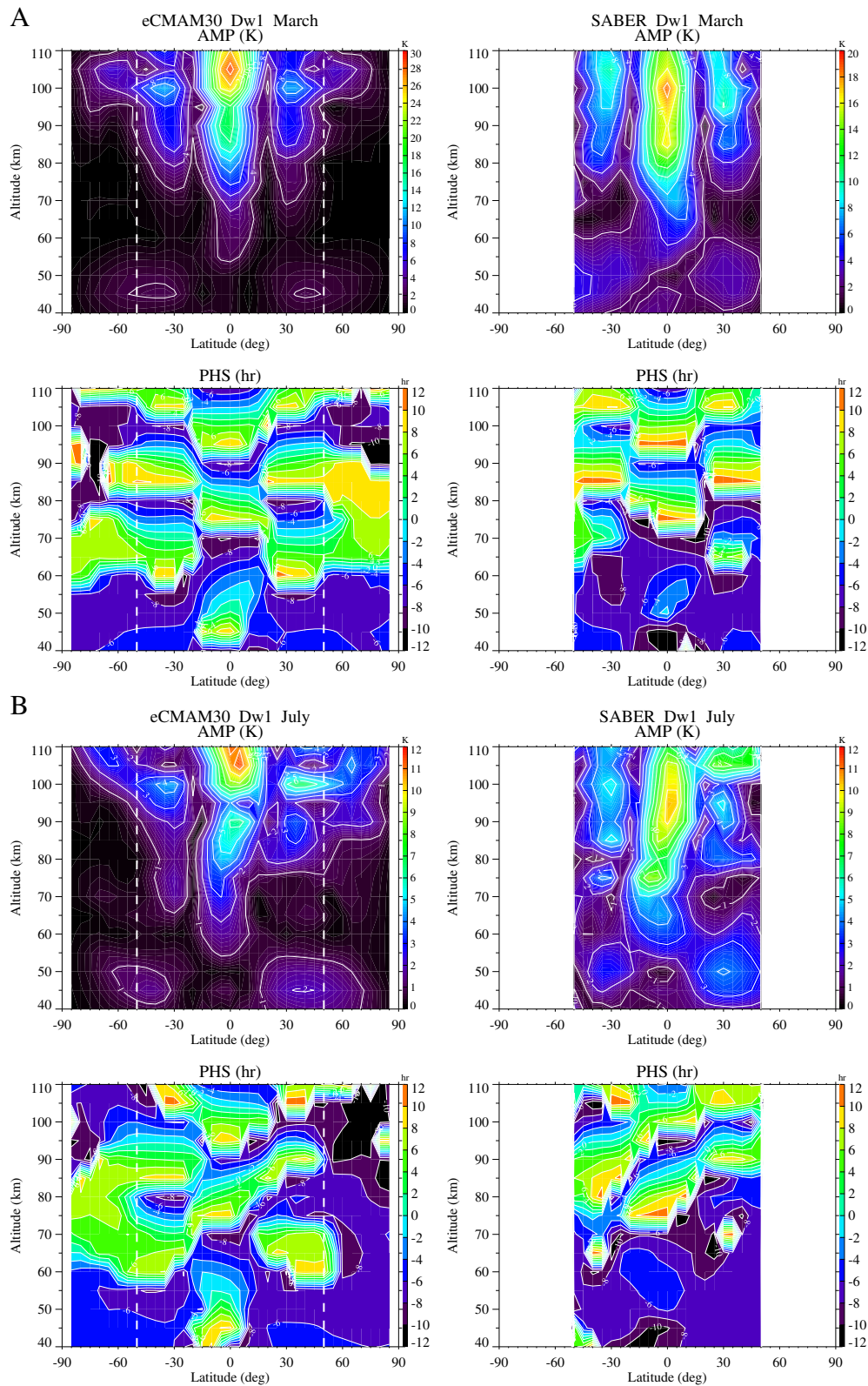


Figure 3 Climatological latitude-altitude cross-sections of temperature amplitude (in Kelvin) and phase (in hour) of Dw1 for March (A) and July (B) from eCMAM30 (left panel) and SABER observation (right panel). White dashed lines denote the latitude 50°N/S. The contour interval is 2 K for March and 1 K for July.

are slightly stronger and broader than their NH counterparts in both datasets. Both maxima correspond to constant phase in eCMAM30 and SABER, which indicates that Dw1 is trapped in situ and cannot propagate upward. This is most likely due to the effects of absorption by solar radiation by ozone, giving rise to an in situ diurnal temperature response that is strongly influenced by the latitudinally broad trapped (nonpropagating or evanescent) diurnal tidal modes (Forbes and Garrett 1979). This local maximum of Dw1 between 40 and 60 km has also been reported by previous satellite data analyses such as those by Forbes and Wu (2006), Forbes et al. (2006), and Zhang et al. (2006).

In July (Figure 3B), the latitudinal structure of Dw1 is more complicated than that in March (Figure 3A). The overall structure is in good agreement between eCMAM30 and SABER. The structure above 60 km is still characterized with an equatorial maximum and two secondary mid-latitude maxima, but some features are different from those in March. The equatorial maximum below 90 km is tilted toward the SH in both eCMAM30 and SABER, and the mid-latitude maximum in each hemisphere contains multiple peaks at different altitudes. Both eCMAM30 and SABER show a three-peak feature in the NH, whereas SABER shows a four-peak feature in the SH and eCMAM30 shows a single peak. The equatorial maximum amplitude is 11 to 12 K for both eCMAM30 and SABER and much weaker than that in March. The secondary maximum amplitude is mainly 3 to 5 K for both eCMAM30 and SABER. The phase decreases with height and compares very good between the model and SABER with less hemispheric symmetry than that in March. The above features indicate combined contributions of both symmetric and asymmetric Hough modes associated with Dw1 in July.

Below 60 km, the structure is still characterized by the mid- and high-latitude maxima in each hemisphere, but hemispheric asymmetry is obvious in both eCMAM30 and SABER. The maximum in NH is much broader than that in the SH. The maximum amplitude in eCMAM30 is about 1 to 2 K, while SABER has a maximum amplitude of 2 to 4 K in this region. The phase stays constant with height and implies that Dw1 is locally trapped.

The nonmigrating tide De3 is primarily excited by latent heating due to deep tropical convection in the troposphere (Forbes et al. 2001). It is shown by Forbes et al. (2006) that the existence of De3 is intimately connected with the predominant wave-4 longitude distribution of topography and land-sea difference at low latitudes. Figure 4 shows the altitude-latitude cross section of temperature amplitude (in Kelvin) and phase (in hour) of De3 for April (a) and August (b). April is the month that De3 reaches moderate amplitude, and August is the month that De3 reaches maximum amplitude in

SABER (more on its seasonal variation in 'Seasonal variations of the diurnal tides'). In April (Figure 4A), both eCMAM30 and SABER show broad maximum feature with strong hemispheric asymmetry in the MLT region. The broad feature extends from 70° S to 60° N and maximizes at 40° to 50° S and 110 km in eCMAM30. There is a secondary maximum located at 10° to 20° S and 100 km. The maximum amplitude of De3 in SABER is located at 10° S and 110 km. Both eCMAM30 and SABER show the broad feature extending to a lower altitude of 75 to 85 km at 0° to 30° N. The maximum amplitude of De3 is stronger in eCMAM30 (17 K) than that in SABER (10 K). The phase structure between eCMAM30 and SABER for April compares very well with decreasing phase with height in the MLT region. The phase in eCMAM30 is more variable than that in SABER due to the more complex amplitude structure.

For De3 in August (Figure 4B), both the latitude-height distribution and the maximum amplitude of the De3 compare very well between eCMAM30 and SABER. The maximum is located between 0° and 30° S in both data and at 105 km in eCMAM30 and 105 to 110 km in SABER. A secondary maximum is present between 30° N and 60° N at 110 km for eCMAM30, while SABER shows a broad feature from 50° S to 50° N. The maximum amplitude of De3 is 18 K for both eCMAM30 and SABER. Another interesting feature is that the maximum feature at 105 km extends to 0° to 30° N at 70 to 80 km and to 0° to 30° S at 40 to 70 km in both eCMAM30 and SABER. The phase is decreasing with height above 75 km and stays constant below 75 km in both data, indicating upward propagating and locally trapped modes, respectively. Similar vertical wavelengths for the observed and modeled De3 are seen in the 80- to 110-km-height region where the amplitudes are largest. Forbes et al. (2006) compared the height versus latitude amplitude distribution of De3 derived from SABER during July and September 2002 with three model results. The three models are the climatological global-scale wave model (GSWM), the GSWM/NCEP (the GSWM utilizes heating rates from the NCAR/NCEP Reanalysis Project), and the Kyushu GCM with full tropospheric physics with heating rates from the NCAR/NCEP reanalysis. All three models predict very similar latitude-height distribution as SABER, but the amplitude is either a factor of 2 too low (GSWM and Kyushu GCM) or 2 too large (GSWM/NCEP). The amplitude peaks at different altitudes for the models and SABER as well. The differences were contributed to possible differences between the De3 vertical wavelengths and molecular viscosity profiles in the models and in the atmosphere.

Figure 5 shows the altitude-latitude cross sections of climatological amplitude and phase of Dw2 in November (a) and of Ds0 in December (b), at which they reach

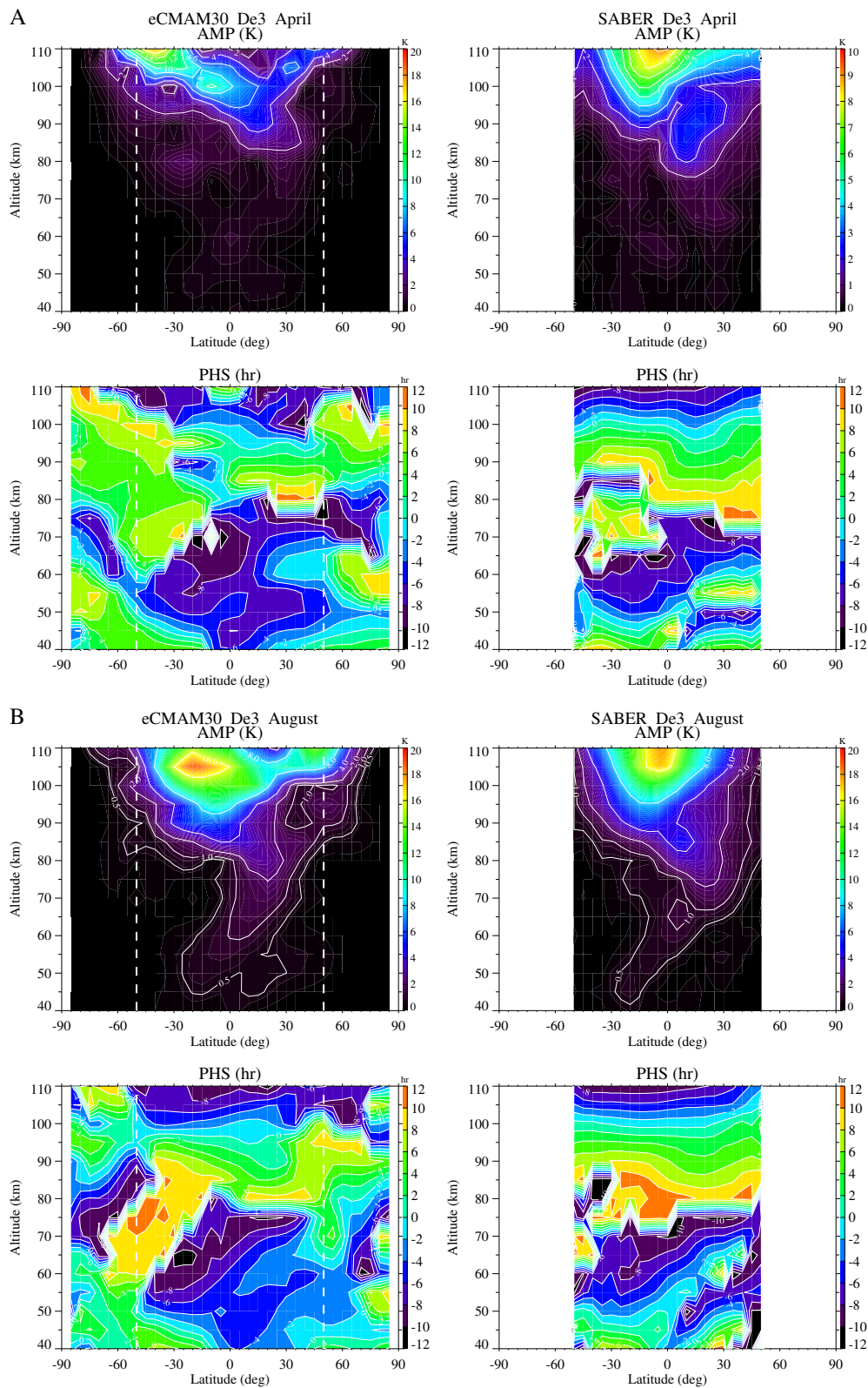


Figure 4 Climatological latitude-altitude cross-sections of temperature amplitude (in Kelvin) and phase (in hour) of De3 for April (A) and August (B) from eCMAM30 (left panel) and SABER observation (right panel). White dashed lines denote the latitude 50°N/S.

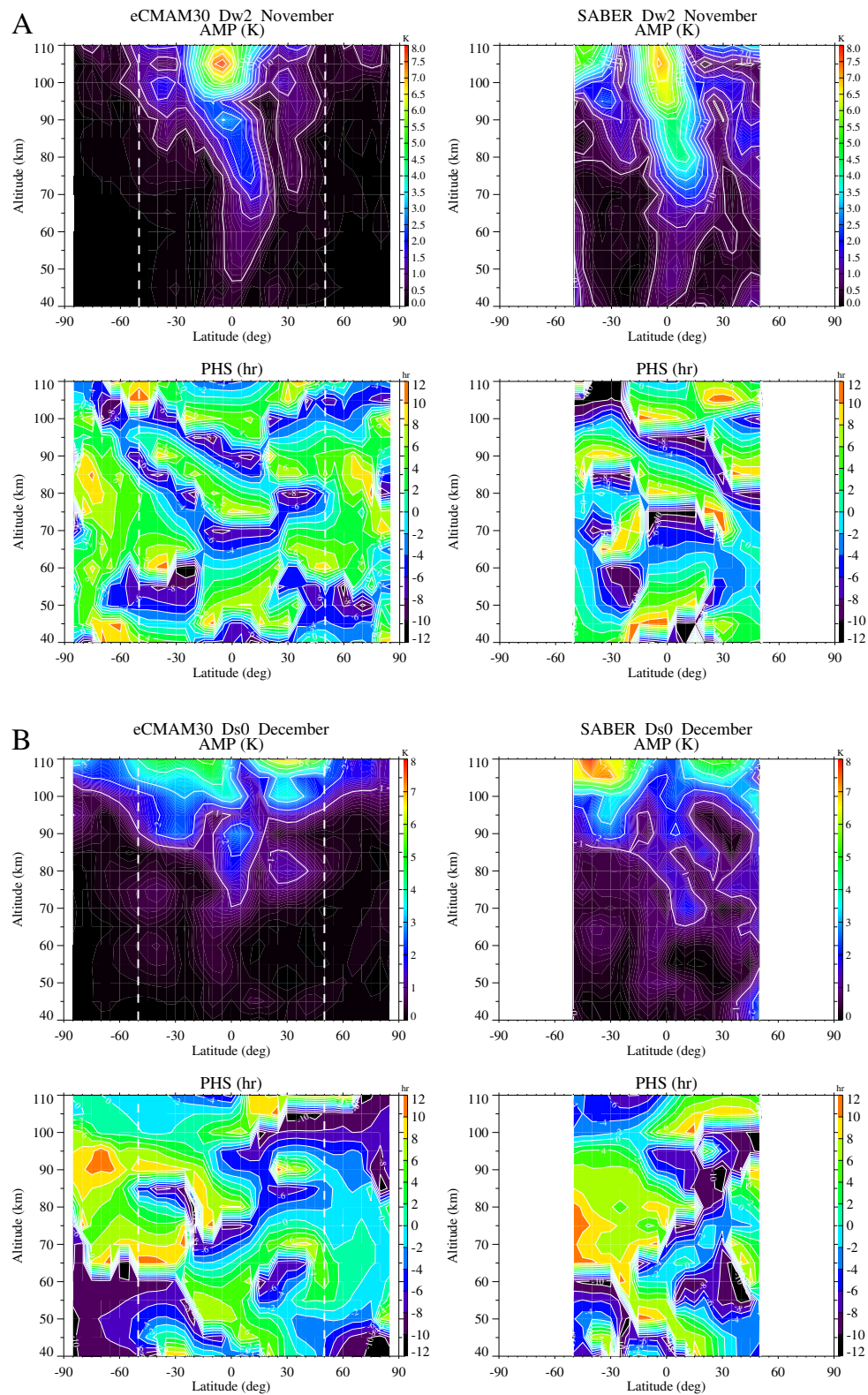


Figure 5 Climatological latitude-altitude cross-sections of temperature amplitude (in Kelvin) and phase (in hour) of Dw2 in November (A) and of Ds0 in December (B) from eCMAM30 (left panel) and SABER observation (right panel). White dashed lines denote the latitude 50°N/S. The contour interval for amplitude is 0.5 K for Dw2 in November, and 1 K for Ds0 in December. The contour interval for phase is 2 h.

their maximum amplitude in both datasets. For Dw2 in November (Figure 5A), both eCMAM30 and SABER present an equatorial maximum which tilts toward the NH between 70 and 90 km and toward the SH below 70 km. The maximum amplitude is located slightly south of the equator in both datasets at 105 km with magnitude of 7 to 8 K. The amplitude between 70 and 90 km is larger in SABER (4 to 5 K) than eCMAM30 (2 to 3 K). The equatorial feature is indicative of propagating modes (Forbes and Wu 2006). There are two secondary mid-latitude maxima in SABER with amplitude approximately 5 K in the SH and 2 to 3 K in the NH, which are not obviously present in eCMAM30. The mid-latitude maxima have also been observed by MLS/UARS at 86 km, which is associated with trapped modes (Forbes and Wu 2006). The phase between the two datasets compares very well: the phase is symmetric about the equator and decreases with height with a vertical wavelength of 25 to 30 km.

For Ds0 in December (Figure 5B), there are two broad maxima located at 0° to 60° of each hemisphere above 100 km for both eCMAM30 and SABER with similar amplitude magnitude of 7 to 8 K. Both eCMAM30 and SABER show hemispheric asymmetry of the amplitude magnitude between the two maxima. The maximum in the SH is slightly stronger than its NH counterpart in SABER, while it is the opposite in eCMAM30. The latitudinal asymmetry was also found in UARS temperature measurements at 86 km (Forbes and Wu 2006) and wind measurements at 95 km (Forbes et al. 2003b). Below 100 km, both datasets show more complex structure: a locally trapped equatorial maximum and two maxima in the mid-latitudes of each hemisphere, which propagate upward. SABER also shows a local maximum at 40 km and 50° N, which has been reported by Xu et al. (2014) as nonlinear interaction effect between the SPW1 and the migrating diurnal tide Dw1. On the other hand, this local maximum is possibly induced by aliasing effect from the nonstationarity of the SPW1 during the fitting interval (Forbes and Wu 2006; Sakazaki et al. 2012), and it is obviously not present in eCMAM30. The phase structures are in good agreement between the two datasets. For the maxima above 100 km, the phase is anti-symmetric about the equator and the phase structure is more variable below 100 km.

Seasonal variations of the diurnal tides

In this section, we present the seasonal variations of the migrating diurnal tide (Dw1) and three nonmigrating diurnal tidal components (De3, Dw2, and Ds0) from eCMAM30 at several representative altitudes and their comparisons with SABER observations.

Figure 6 illustrates the seasonal variations of Dw1 temperature amplitude and phase at 95 km (a) and 45

km (b) from both eCMAM30 and SABER. At 95 km (Figure 6A), both eCMAM30 and SABER show that the amplitude of the Dw1 in the MLT region exhibits a strong semiannual variation, which is characterized by equinoctial maxima and solstitial minima. This semiannual variation is well documented in both ground-based and previous satellite observations (Vincent et al. 1998; Fritts and Isler 1994; Hays and Wu 1994; Burrage et al. 1995; McLandress et al. 1996; Zhang et al. 2006). Three explanations have been proposed for the semiannual variation of Dw1: semiannual variation in the heating that forces the tide (Lieberman et al. 2003; Hagan and Forbes 2002; Xu et al. 2010), variation of the background winds in the tropical stratosphere and mesosphere (McLandress 2002a, b), and variations due to damping within the MLT region (Xu et al. 2009a; Lieberman et al. 2010).

Both eCMAM30 and SABER show that the spring maximum (16 to 18 K) is slightly stronger than the autumn maximum (12 to 16 K). The magnitude of the equinox maxima is in agreement with previous SABER analysis (Zhang et al. 2006). SABER has much stronger amplitude (10 K for the equatorial maximum and 4 K for the mid-latitude maxima) during solstitial minima than eCMAM30 (2 K for both equatorial and mid-latitude maxima) at 95 km. The magnitude of the two mid-latitude maxima is similar in eCMAM30, while the NH mid-latitude maximum tends to be stronger than the SH counterpart in SABER. Moreover, Dw1 exhibits an annual variation in the Polar Regions in eCMAM30, which has also been reported in Du et al. (2014) from the free-running eCMAM.

The phase of Dw1 is symmetric about the equator and less variable than its amplitude at 95 km in both datasets. In the equatorial region, the phase is approximately 8 to 10 LT all year round in eCMAM30, while it is 2 h ahead (10 to 12 LT) in SABER. Both eCMAM30 and SABER show that the phase difference between the equatorial region and the mid-latitudes is approximately 12 h. At mid-latitudes, the phase from eCMAM30 exhibits an annual variation with phase varying from approximately 0 LT during January and December (May and June) to 10 to 12 LT during June to September (February to April) in the SH (NH). SABER shows similar annual variation but the phase is 2 to 4 h ahead.

Figure 6B shows the seasonal variation of Dw1 at 45 km from both eCMAM30 and SABER. There is a clear annual variation in the amplitude of Dw1 at 45 km. It is a broad feature from 15° to 20° N (S) to 80° N (S) during nonwinter months with amplitude of 2 to 3 K. During winter months (November, December, and January in NH and May to August in SH), this feature shrieks in latitudinal coverage to 30° to 60° N (S) with amplitude of 2 K. The latitudinal structure of Dw1 at 45 km within 50° N/S from SABER compares well with eCMAM30

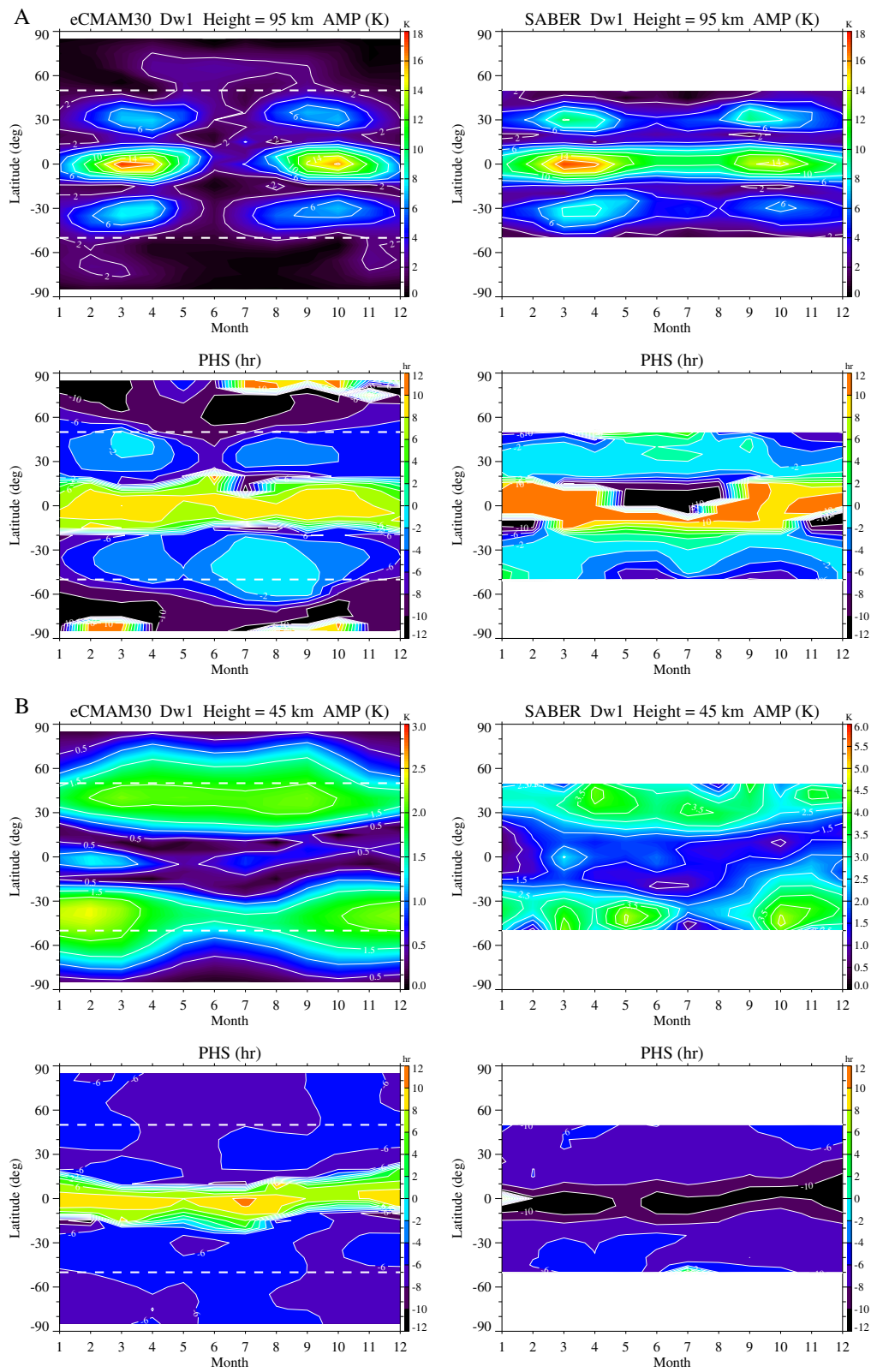


Figure 6 Seasonal variations of climatological temperature amplitude (in Kelvin) and phase (in hours) of Dw1 at 95 km (A) and 45 km (B) from eCMAM30 (left panel) and SABER observations (right panel). White dashed lines denote the latitudes of 50°S and 50°N.

but with multiple peaks (April in NH and March, May, and October in SH). The maximum amplitude in SABER can reach 5 to 6 K, which is larger than that in eCMAM30 at this altitude. Both eCMAM30 and SABER show an equatorial maximum during March although it starts earlier in eCMAM30 (February) than in SABER.

The phase compares well between the two datasets at 45 km. Phase structure shows little variation (less than 2 h difference) over the year at all latitudes from both eCMAM30 and SABER. The magnitude is approximately 6 LT in both eCMAM30 and SABER in the mid-latitudes of each hemisphere. The phase at the equatorial region is about 4 h difference from the mid-latitude phase in SABER and 6 h difference in eCMAM30.

The seasonal variations of three nonmigrating diurnal tides De3 (a), Dw2 (b), and Ds0 (c) at the altitude where their maximum is located are presented in Figure 7. For De3 at 105 km (Figure 7A), the seasonal variation is dominated by an annual variation in SABER with amplitude reaching maximum (12 K) between June and October and minimum between December and March (<4 K). SABER De3 distribution is symmetric-like about 10° S latitude. These features are in agreement with previous SABER analysis (Zhang et al. 2006). There are some differences between eCMAM30 and SABER on seasonal variation of De3. The model shows a strong NH winter maximum between 5° N and 10° S, which is not present in SABER, which might imply that eCMAM overestimates the latent heat release during this season. Other maxima are located at 5° N to 5° S in September and 10° to 30° S in July in eCMAM30. The magnitude for the NH summer maximum is similar between eCMAM30 and SABER. For the broad maximum between March and November, the phase varies between 16 and 20 LT in both SABER and eCMAM30. The phase between December and February is different between the two datasets due to the amplitude difference during this period.

For Dw2 at 105 km (Figure 7B), the seasonal variation in eCMAM30 is dominated as a semiannual variation with maximum in March and October and minimum in January, June, and July. The maximum in October (9 to 10 K) is slightly larger than that in March (7 to 8 K) in eCMAM30. There is an annual variation with the latitudinal structure of Dw2 in eCMAM30. The maximum is located at between 5° N and 20° S between September and March and at 5° S to 20° N between April and August. The seasonal variation in SABER is dominated by an annual variation with maximum amplitude in September-April and minimum amplitude in May-August. The maximum amplitude is similar between the two datasets with eCMAM30 maximum (9 to 10 K) slightly larger than SABER (7 to 8 K). The annual variation of the latitudinal structure of Dw2 as seen in eCMAM30 is not present in SABER. Besides the equatorial maximum, there are

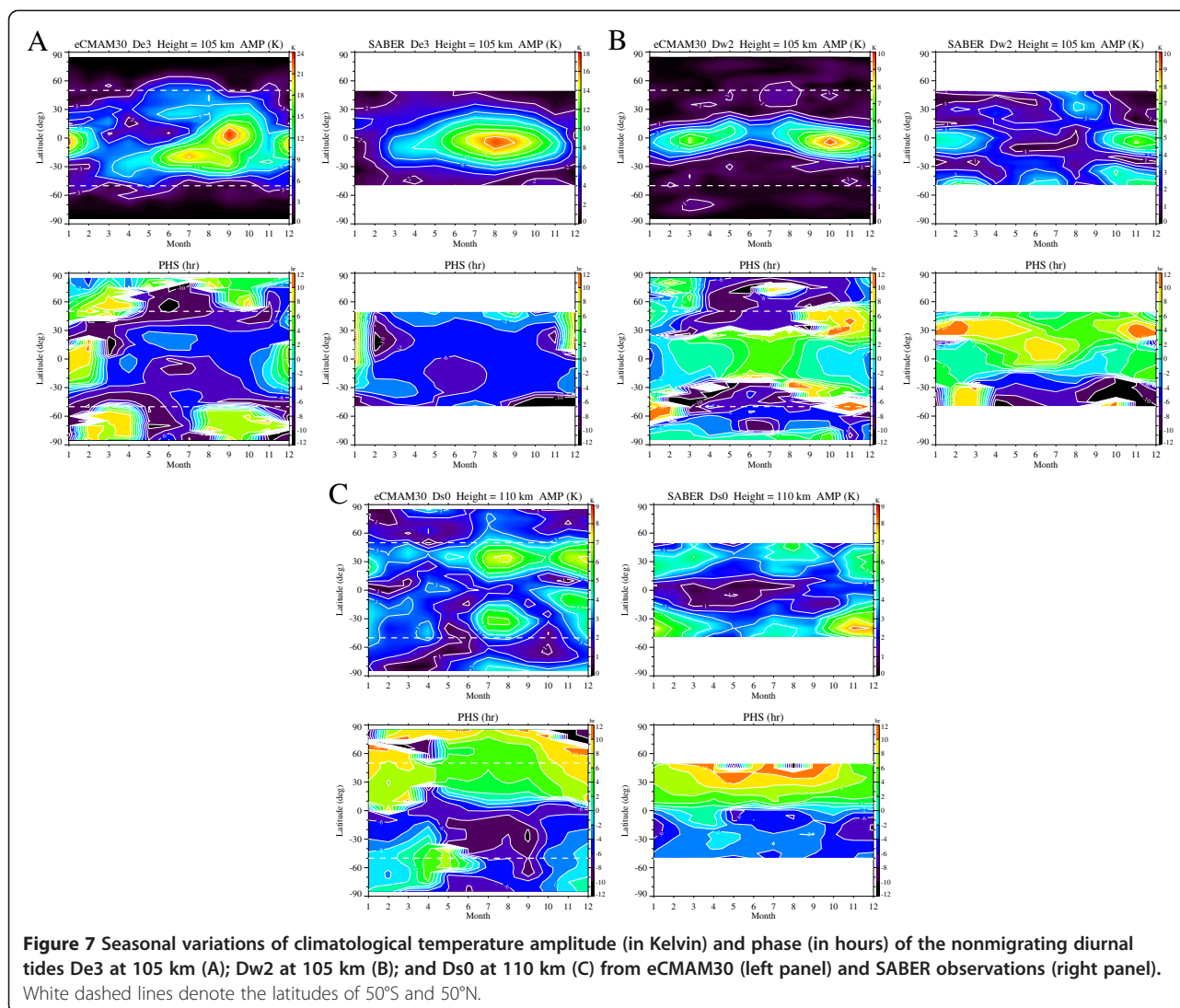
also multiple peaks in mid-latitudes (August in NH and February-March, June, and November in SH) from SABER, which are not present in eCMAM30. The phases associated with the equatorial maximum in eCMAM30 and SABER both present an annual variation. The phase is 22 to 24 LT during September and March, and 2 to 4 LT during April and August in eCMAM30 and SABER is about 6 h ahead of eCMAM30 all year round.

For Ds0 at 110 km (Figure 7C), the seasonal variation of Ds0 agrees very well between eCMAM30 and SABER. Both datasets present multiple peaks that are centered on 30° N/S. The timing of the maxima is consistent between the two datasets. The maxima are symmetric about the equator and are present during October-March and June-September. The magnitude of the maxima (7 to 9 K) is very similar between eCMAM30 and SABER as well. The relative strength of the peaks is slightly different: eCMAM30 shows that the NH peaks are stronger than their southern counterparts while SABER shows the opposite during October-March. The phase between the two datasets also compares very well. The phase is anti-symmetric about the equator with little variation all year round. In the NH (SH), the phase is about 2 (14) to 8 (18) LT.

Interannual variations of the diurnal tides

Long-term tidal variability did not receive much attention up to now. Indeed, to study it, long time series of observations or model runs are needed. This practically excluded its study in the middle and upper atmosphere until recently. There are two potentially important natural internal sources of long-term tidal variability in our atmosphere: the El Niño-Southern Oscillation (ENSO) and the stratospheric quasi-biennial oscillation (QBO). With the large variations in the rainfall and latent heat patterns caused by ENSO, it is to be expected that it will have a noticeable effect on the tides. A few studies have investigated the role of the ENSO (Vial et al. 1994; Gurubaran et al. 2005; Lieberman et al. 2007; Pedatella and Liu 2012, 2013; Warner and Oberheide 2014) and QBO (Vincent et al. 1998; Hagan et al. 1999; Mayr and Mengel 2005; Wu et al. 2008a, b; Xu et al. 2009b; Oberheide et al. 2009; Gurubaran et al. 2009; Wu et al. 2011) on driving interannual tidal variability. However, a comprehensive view of the tidal change that occurs in response to the ENSO and QBO is still lacking.

A common deficiency suffered by many free-running GCMs is the absence of a QBO. By nudging wind and temperature to the reanalysis data in the troposphere and stratosphere, the eCMAM is able to produce the stratospheric QBO (not shown), thus allowing a more realistic interaction between the atmospheric tides and background atmosphere. The sea surface temperature (SST) in the model is subscribed to monthly global



complete fields of SST and sea ice concentration at each latitude-longitude grid from the Met Office Hadley Center's sea ice and sea surface temperature dataset (HadISST) during the same time period of 1979 to 2010. Therefore, ENSO is also included in the model in a realistic way. A major advantage of using data-assimilated middle atmosphere models such as eCMAM30 to study interannual variation of the atmospheric tides is to have many available variables (296 in the case of eCMAM30) that are self-consistently generated and regularly saved at even spatial and temporal grids. This complete dataset enables a comprehensive evaluation on the momentum and energy budget of the atmospheric tides and its relationship with natural variability in the atmosphere such as ENSO and QBO. Here, we present a simple validation of the interannual time series of two dominant diurnal tides (Dw1 and De3) from eCMAM30 against SABER at the overlapped data period (January 2002 to June 2010).

The monthly mean temperature amplitude of Dw1 at 95 km from both eCMAM30 and SABER is illustrated in Figure 8 for the period of January 2002 to June 2010. As seen in previous sections, the climatological latitudinal-altitudinal structure and seasonal variation of Dw1 from eCMAM30 are in excellent agreement with SABER. From Figure 8A, the amplitude of Dw1 clearly presents a strong interannual variation. The March and September equinox maxima are stronger in the years of 2002, 2004, 2006, and 2008 in both eCMAM30 and SABER than other years. Figure 8B presents the interannual anomaly time series and its Fourier spectrum at the equator and 95 km from eCMAM30 (red) and SABER (blue). The interannual anomaly is calculated by subtracting the annual mean and seasonal variation from the original time series. The interannual anomaly can reach -10 K to $+10$ K for eCMAM30 and is slightly weaker in SABER (from -5 K to $+9$ K). The Dw1 in years of 2003,

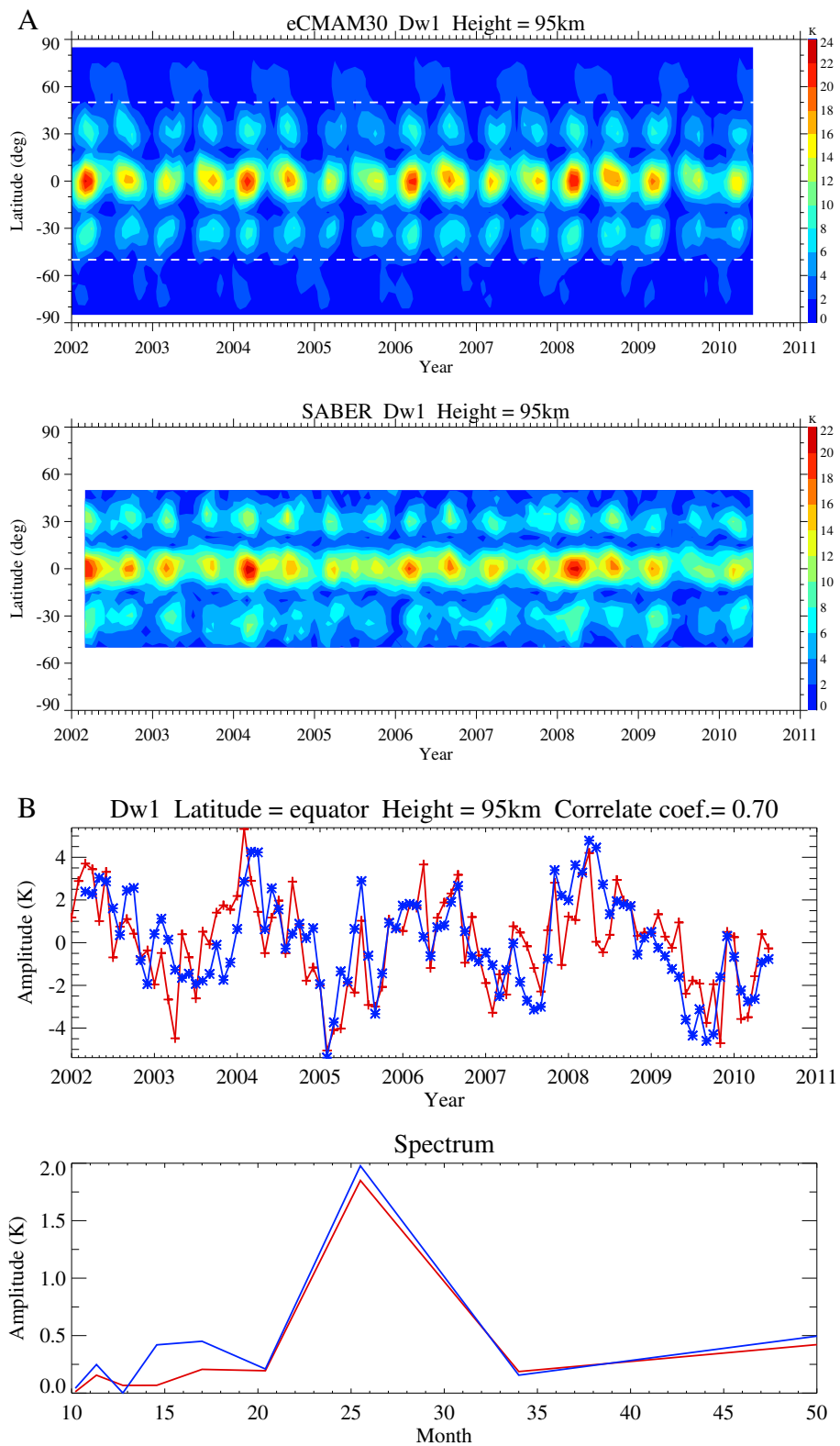


Figure 8 (A) Inter-annual variation of Dw1 amplitude at 95 km as a function of latitude from eCMAM30 (top) and SABER (bottom) for the period of January 2002 to June 2010. White dashed lines denote 50°S and 50°N. (B) Interannual amplitude anomaly of Dw1 above equator at 95 km (top) and its amplitude spectrum (bottom) from eCMAM30 (red) and SABER (blue).

2005, 2007, and 2009 has weaker amplitude than the climatology. The anomaly between eCMAM30 and SABER follows closely and the correlation between the two datasets is 0.7. The Fourier spectrum of the interannual anomaly has a peak at 25 to 26 months from both eCMAM30 and SABER with amplitude greater than 1.5 K, which is likely associated with equatorial QBO of background zonal wind in the stratosphere.

Figure 9 is similar to Figure 8, but for the interannual variation of De3 at 105 km. The discrepancies associated with seasonal variation of De3 are obvious between the model and SABER. As mentioned in 'Seasonal variations of the diurnal tides,' the January maximum presented in the model is not seen in SABER. At 105 km (Figure 9A), SABER shows stronger De3 amplitude in 2002, 2004, 2006, and 2008 than in other years. On the other hand, eCMAM30 presents strongest De3 amplitude in 2002 and stronger amplitude in 2004 and 2006. The 2-year cycle is interrupted in eCMAM30 for 2008 and its amplitude is not as strong as those for 2004 and 2006. The correlation of the interannual anomaly time series from eCMAM30 and SABER is 0.49 for De3 at the equator and 105 km. The Fourier spectrum of the time series from SABER (blue line in Figure 9B) shows a peak at 11 to 12 months and another peak at 25 to 26 months, while the spectrum from eCMAM30 (red line) shows a peak at 16 to 17 months and another one at 25 to 26 months. The amplitude spectrum peak at 25 to 26 months presented in both SABER and eCMAM30 is likely associated with QBO in the stratosphere. The cause of the interannual variation and its relationship to QBO and ENSO will be investigated in more detail in a separate paper.

Conclusions

The newly nudged eCMAM30 temperature data (from January 1979 to June 2010) is used to study the climatology of background mean temperature and diurnal tides in the stratosphere and MLT region. The modeled background mean temperature and diurnal tides are validated against the diurnal tidal climatology observed from SABER for the last decade (from January 2002 to December 2013).

For the background mean temperature, the model reproduces the latitudinal temperature gradients quite well. The main difference is that the cold mesopause in the model is about 10 to 20 K colder than that in SABER, which is a common problem associated with GCMs with insufficient gravity wave forcing. For the diurnal tidal spectrum, the tidal composition and their relative strength agree very well between the two datasets in both the stratosphere and MLT regions. During the NH spring, the migrating Dw1 component has the largest amplitude while the nonmigrating De3 component is the second largest. During the NH summer, Dw1 has the largest

amplitude below 65 km while De3 becomes the strongest in the upper MLT region although the model and SABER disagree on the exact altitude for this changeover. The spectrum is richer in NH summer than NH spring due to the weaker amplitude of Dw1.

The climatological altitude-latitude structures of the migrating diurnal tide Dw1 and three nonmigrating diurnal tides De3, Dw2, and Ds0 from the eCMAM30 and SABER are generally in very good agreement. Besides the better-known feature associated with Dw1 in the MLT region, the model reproduces the observed trapped local maximum between 40 and 60 km very well. In addition to the good agreement above 90 km, the altitude-latitude structure of De3 in August between 40 and 90 km (with amplitude <4 K) also compares well between the model and SABER. Similar characteristics are also found for the altitude-latitude structure of Dw2 and Ds0. The phase and vertical wavelength of the tidal components presented are also in very good agreement between the model and SABER.

The seasonal variations of the diurnal tidal components compare well between the model and SABER. The semi-annual variation at 95 km and the annual variation at 45 km associated with Dw1 observed in SABER are well represented in the model. For Ds0, both datasets present multiple peaks with consistent timing for these peaks. The largest discrepancy associated with the seasonal variation between the model and SABER occurs with De3. Besides the NH summer maximum presented in both eCMAM30 and SABER, the model also shows a maximum during NH winter (December-February), which is not present in SABER. This might imply that the model is overestimating the latent heat release during NH winter.

The interannual time series of Dw1 and De3 are also shown from both datasets for the period of January 2002 and June 2010. Spectral analysis of the interannual variability reveals a strong peak at 25 to 26 months in both eCMAM30 and SABER, which indicates the modulation of diurnal tides by the stratospheric QBO. A detailed study of the interannual variability of the tides with this dataset will be pursued in more details in the future.

Overall, we consider the climatology of the diurnal tides simulated by the eCMAM30 to agree very well with the observations, although there are some differences. The data-assimilated eCMAM does perform better than the free-running version of the model in terms of simulating more realistic tidal amplitude and phase. The form of the model parameterization schemes relevant to tidal forcing (such as latent heat release and/or the convective parameterizations) and dissipation (associated with parameterized gravity waves) play a major role in the form of the eCMAM results and are potential sources for these discrepancies. Another potential source is differences between the background fields of the model

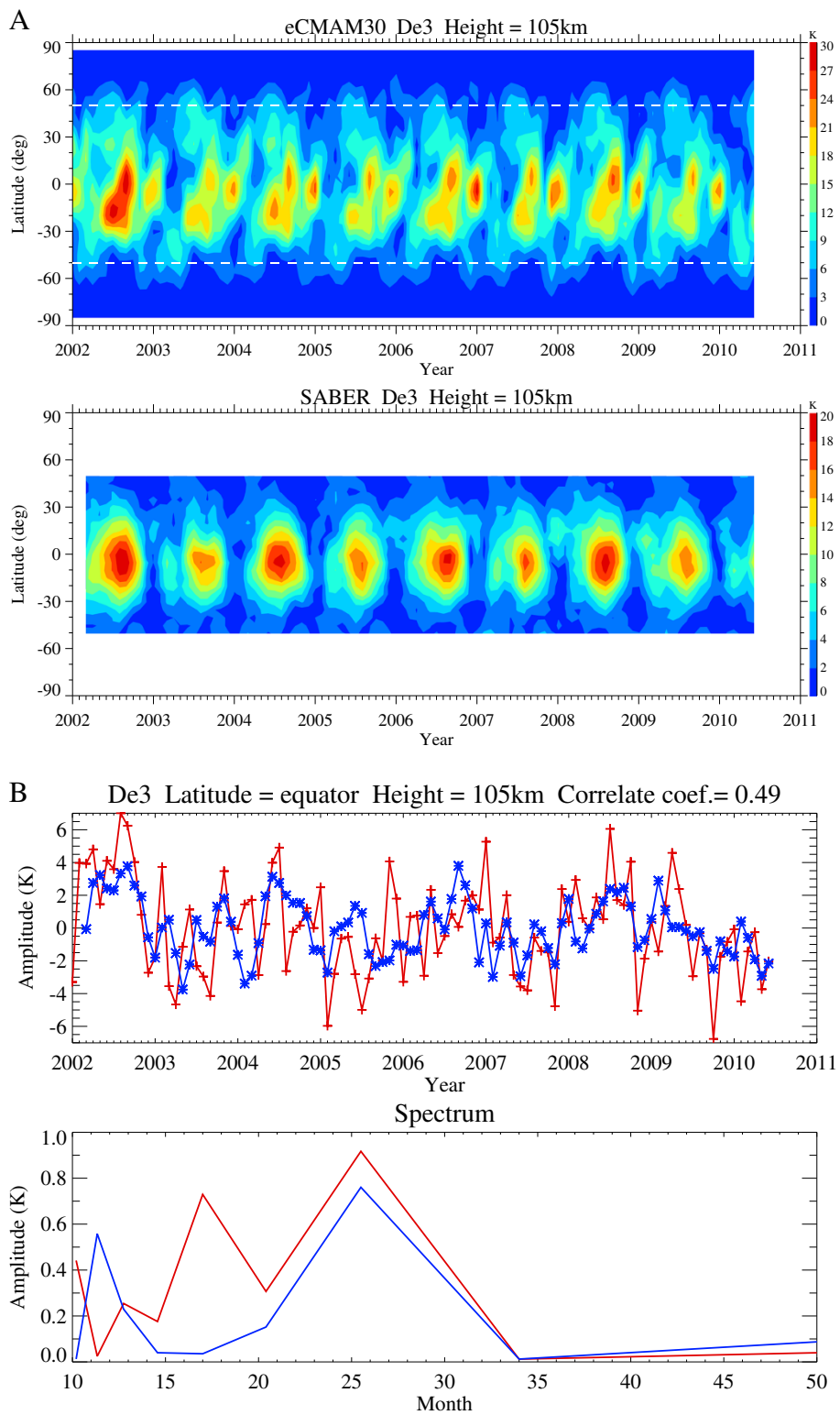


Figure 9 Same as Figure 8, but for De3 at 105 km.

and the real atmosphere, which affect the filtering of and nonlinear interactions between components. The investigation of these dependencies requires more extensive observations and model analyses and is certain to be the subject of future investigations. More work is required to understand and refine tidal source mechanisms, in particular latent heat release and convective parameterizations, in order to improve model simulations.

Endnotes

^aThroughout paper, we utilize the notation Dws or Des to denote a westward or eastward propagating diurnal tide, respectively, with zonal wave number s . The standing oscillations are denoted as $Ds0$. Of these tidal components, $Dw1$ is the migrating tides and the rest are nonmigrating tides.

Competing interests

The authors declare they have no competing interests.

Authors' contributions

JD, WEW, SRB, and VIF carried out the eCMAM30 study for diurnal tides. QG and SZ carried out the SABER observation study for diurnal tides. All authors read and approved the final manuscript.

Acknowledgements

The authors would like to thank Dr. Jia Yue from Hampton University and Dr. Anne Smith from NCAR for their helpful comments on the manuscript. Quan Gan was funded by the College of Arts and Science, University of Louisville, and by the National Natural Science Foundation of China (grant 41304120) and National Basic Research Program of China (grant 2012CB825605). Jian Du was funded by NSF CEDAR grant AGS-1243019. William E Ward was supported by the Natural Sciences and Engineering Council (NSERC) and the Canadian Foundation for Climate and Atmospheric Science (CFCAS). Stephen R Beagley and Victor I Fomichev were supported by the Canadian Space Agency. Shaodong Zhang was supported by the National Basic Research Program of China (grant 2012CB825605).

Author details

¹Department of Physics and Astronomy, University of Louisville, Louisville, KY 40292, USA. ²Department of Physics, University of New Brunswick, Fredericton, NB E3B 5A3, Canada. ³Centre for Research in Earth and Space Science, York University, Toronto, ON M3J 1P3, Canada. ⁴School of Electronic Information, Wuhan University, Wuhan, China.

Received: 31 March 2014 Accepted: 16 August 2014

Published: 28 August 2014

References

- Beagley SR, McLandress C, Fomichev VI, Ward WE (2000) The extended Canadian middle atmosphere model. *Geophys Res Lett* 27(16):2529–2532, doi:10.1029/1999gl012333
- Beagley SR, McConnell JC, Fomichev VI, Semeniuk K, Jonsson AI, Garcia Munoz A, McLandress C, Shepherd TG (2007) Extended CMAM: Impacts of Thermospheric Neutral and Ion Chemistry on the Middle Atmosphere, AGU, fall
- Beagley SR, Boone CD, Fomichev VI, Jin JJ, Semeniuk K, McConnell JC, Bernath PF (2010) First multi-year occultation observations of CO₂ in the MLT by ACE satellite: observations and analysis using the extended CMAM. *Atmos Chem Phys* 10(3):1133–1153, doi:10.5194/acp-10-1133-2010
- Burrage MD, Wu DL, Skinner WR, Ortland DA, Hays PB (1995) Latitude and seasonal dependence of the semidiurnal tide observed by the high-resolution Doppler imager. *J Geophys Res-Atmos* 100(D6):11313–11321, doi:10.1029/95jd00696
- Chang LC, Ward WE, Palo SE, Du J, Wang DY, Liu HL, Hagan ME, Portnyagin Y, Oberheide J, Goncharenko LP, Nakamura T, Hoffmann P, Singer W, Batista P, Clemesha B, Manson AH, Riggan DM, She CY, Tsuda T, Yuan T (2012) Comparison of diurnal tide in models and ground-based observations during the 2005 equinox CAWSES tidal campaign. *J Atmos Sol-Terr Phys* 78–79:19–30, doi:10.1016/j.jastp.2010.12.010
- Chapman S, Lindzen RS (1970) *Atmospheric Tides: Thermal and Gravitational*. Gordon and Breach, New York
- Coll MAI, Forbes JM (1998) Dynamical influences on atomic oxygen and 5577 angstrom emission rates in the lower thermosphere. *Geophys Res Lett* 25(4):461–464
- Coll MAI, Forbes JM (2002) Nonlinear interactions in the upper atmosphere: the $s = 1$ and $s = 3$ nonmigrating semidiurnal tides. *J Geophys Res* 107(A8): doi:10.1029/2001ja900179
- Davis RN, Du J, Smith AK, Ward WE, Mitchell NJ (2013) The diurnal and semidiurnal tides over Ascension Island (8 degrees S, 14 degrees W) and their interaction with the stratospheric quasi-biennial oscillation: studies with meteor radar, eCMAM and WACCM. *Atmos Chem Phys* 13(18):9543–9564, doi:10.5194/acp-13-9543-2013
- de Grandpre J, Beagley SR, Fomichev VI, Griffioen E, McConnell JC, Medvedev AS, Shepherd TG (2000) Ozone climatology using interactive chemistry: results from the Canadian Middle Atmosphere Model. *J Geophys Res-Atmos* 105 (D21):26475–26491, doi:10.1029/2000jd900427
- Dee DP, Uppala SM, Simmons AJ, Berrisford P, Poli P, Kobayashi S, Andrae U, Balmaseda MA, Balsamo G, Bauer P, Bechtold P, Beljaars ACM, van de Berg L, Bidlot J, Bormann N, Delsol C, Dragani R, Fuentes M, Geer AJ, Haimberger L, Healy SB, Hersbach H, Holm EV, Isaksen I, Kallberg P, Kohler M, Matricardi M, McNally AP, Monge-Sanz BM, Morcrette JJ, Park BK, Peubey C, de Rosnay P, Tavolato C, Thepaut JN, Vitart F (2011) The ERA-Interim reanalysis: configuration and performance of the data assimilation system. *Q J Roy Meteor Soc* 137(656):553–597, doi:10.1002/qj.828
- Du J (2008) *Mesosphere and Lower Thermosphere Dynamics Study using the Extended Canadian Middle Atmosphere Model (CMAM)*, Ph.D. thesis. University of New Brunswick, Canada
- Du J, Ward WE (2010) Terdiurnal tide in the extended Canadian Middle Atmospheric Model (CMAM). *J Geophys Res-Atmos* 115: doi:10.1029/2010jd014479
- Du J, Ward WE, Oberheide J, Nakamura T, Tsuda T (2007) Semidiurnal tides from the extended Canadian Middle Atmosphere Model (CMAM) and comparisons with TIMED Doppler interferometer (TID) and meteor radar observations. *J Atmos Sol-Terr Phys* 69(17–18):2159–2202, doi:10.1016/j.jastp.2007.07.014
- Du J, Ward WE, Cooper FC (2014) The character of polar tidal signatures in the extended Canadian Middle Atmosphere Model (eCMAM). *J Geophys Res-Atmos* 119.
- England SL (2012) A review of the effects of non-migrating atmospheric tides on the Earth's low-latitude ionosphere. *Space Sci Rev* 168(1–4):211–236, doi:10.1007/s11214-011-9842-4
- Fomichev VI, Ward WE, Beagley SR, McLandress C, McConnell JC, McFarlane NA, Shepherd TG (2002) Extended Canadian Middle Atmosphere Model: zonal-mean climatology and physical parameterizations. *J Geophys Res-Atmos* 107 (D10): doi:10.1029/2001jd000479
- Forbes JM (1982) Atmospheric Tides .1. Model description and results for the solar diurnal component. *J Geophys Res* 87(Na7):5222–5240, doi:10.1029/Ja087ia07p05222
- Forbes JM, Garrett HB (1979) Theoretical studies of atmospheric tides. *Rev Geophys* 17(8):1951–1981, doi:10.1029/Rg017i008p01951
- Forbes JM, Wu D (2006) Solar tides as revealed by measurements of mesosphere temperature by the MLS experiment on UARS. *J Atmos Sci* 63(7):1776–1797, doi:10.1175/Jas3724.1
- Forbes JM, Roble RG, Fesen CG (1993) Acceleration, heating, and compositional mixing of the thermosphere due to upward propagating tides. *J Geophys Res* 98(A1):311–321, doi:10.1029/92ja00442
- Forbes JM, Hagan ME, Zhang X, Hamilton K (1997) Upper atmosphere tidal oscillations due to latent heat release in the tropical troposphere. *Ann Geophys-Atm Hydr* 15(9):1165–1175, doi:10.1007/s00585-997-1165-0
- Forbes JM, Palo SE, Zhang XL (2000) Variability of the ionosphere. *J Atmos Sol-Terr Phys* 62(8):685–693, doi:10.1016/S1364-6826(00)00029-8
- Forbes JM, Zhang XL, Hagan ME (2001) Simulations of diurnal tides due to tropospheric heating from the NCEP/NCAR Reanalysis Project. *Geophys Res Lett* 28(20):3851–3854, doi:10.1029/2001gl013500
- Forbes JM, Hagan ME, Miyahara S, Miyoshi Y, Zhang XL (2003a) Diurnal nonmigrating tides in the tropical lower thermosphere. *Earth Planets Space* 55(7):419–426
- Forbes JM, Zhang XL, Talaat ER, Ward W (2003b) Nonmigrating diurnal tides in the thermosphere. *J Geophys Res* 108(A1): doi:10.1029/2002ja009262
- Forbes JM, Russell J, Miyahara S, Zhang X, Palo S, Mlynczak M, Mertens CJ, Hagan ME (2006) Troposphere-thermosphere tidal coupling as measured by the

- SABER instrument on TIMED during July-September 2002. *J Geophys Res* 111 (A10): doi:10.1029/2005ja011492
- Fritts DC, Isler JR (1994) Mean motions and tidal and 2-day structure and variability in the mesosphere and lower thermosphere over Hawaii. *J Atmos Sci* 51 (14):2145–2164, doi:10.1175/1520-0469(1994)051<2145:Mmatat>2.0.Co;2
- Fritts DC, Vincent RA (1987) Mesospheric momentum flux studies at Adelaide, Australia - observations and a gravity wave-tidal interaction model. *J Atmos Sci* 44(3):605–619, doi:10.1175/1520-0469(1987)044<0605:Mmsaa>2.0.Co;2
- Gan Q, Zhang SD, Yi F (2012) TIMED/SABER observations of lower mesospheric inversion layers at low and middle latitudes. *J Geophys Res-Atmos* 117: doi:10.1029/2012jd017455
- Gong Y, Zhou QH, Zhang SD (2013) Atmospheric tides in the low-latitude E and F regions and their responses to a sudden stratospheric warming event in January 2010. *J Geophys Res* 118(12):7913–7927, doi:10.1002/2013ja019248
- Grieger N, Volodin EM, Schmitz G, Hofmann P, Manson AH, Fritts DC, Igarashi K, Singer W (2002) General circulation model results on migrating and nonmigrating tides in the mesosphere and lower thermosphere. Part I: comparison with observations. *J Atmos Sol-Terr Phys* 64(8–11):897–911, doi:10.1016/S1364-6826(02)00045-7
- Grieger N, Schmitz G, Achatz U (2004) The dependence of the nonmigrating diurnal tide in the mesosphere and lower thermosphere on stationary planetary waves. *J Atmos Sol-Terr Phys* 66(6–9):733–754, doi:10.1016/j.jastp.2004.01.022
- Gurubaran S, Rajaram R, Nakamura T, Tsuda T (2005) Interannual variability of diurnal tide in the tropical mesopause region: a signature of the El Niño-Southern Oscillation (ENSO). *Geophys Res Lett* 32(13): doi:10.1029/2005gl022928
- Gurubaran S, Rajaram R, Nakamura T, Tsuda T, Riggan D, Vincent RA (2009) Radar observations of the diurnal tide in the tropical mesosphere-lower thermosphere region: longitudinal variabilities. *Earth Planets Space* 61(4):513–524
- Hagan ME (1996) Comparative effects of migrating solar sources on tidal signatures in the middle and upper atmosphere. *J Geophys Res-Atmos* 101(D16):21213–21222, doi:10.1029/96jd01374
- Hagan ME, Forbes JM (2002) Migrating and nonmigrating diurnal tides in the middle and upper atmosphere excited by tropospheric latent heat release. *J Geophys Res-Atmos* 107(D24): doi:10.1029/2001jd001236
- Hagan ME, Roble RG (2001) Modeling diurnal tidal variability with the National Center for Atmospheric Research thermosphere-ionosphere-mesosphere-electrodynamics general circulation model. *J Geophys Res* 106(A11):24869–24882, doi:10.1029/2001ja000057
- Hagan ME, Forbes JM, Vial F (1995) On modeling migrating solar tides. *Geophys Res Lett* 22(8):893–896, doi:10.1029/95gl00783
- Hagan ME, Burrage MD, Forbes JM, Hackney J, Randel WJ, Zhang X (1999) QBO effects on the diurnal tide in the upper atmosphere. *Earth Planets Space* 51 (7–8):571–578
- Hagan ME, Maute A, Roble RG (2009) Tropospheric tidal effects on the middle and upper atmosphere. *J Geophys Res Atmos* 114(A01302): doi:10.1029/2008JA013637
- Hays PB, Wu DL (1994) Observations of the diurnal tide from space. *J Atmos Sci* 51(20):3077–3093, doi:10.1175/1520-0469(1994)051<3077:Ootdtf>2.0.Co;2
- Hines CO (1997a) Doppler-spread parameterization of gravity-wave momentum deposition in the middle atmosphere. 1. Basic formulation. *J Atmos Sol-Terr Phys* 59(4):371–386, doi:10.1016/S1364-6826(96)00079-X
- Hines CO (1997b) Doppler-spread parameterization of gravity-wave momentum deposition in the middle atmosphere. 2. Broad and quasi monochromatic spectra, and implementation. *J Atmos Sol-Terr Phys* 59(4):387–400, doi:10.1016/S1364-6826(96)00080-6
- Huang FT, Reber CA (2004) Nonmigrating semidiurnal and diurnal tides at 95 km based on wind measurements from the High Resolution Doppler Imager on UARS. *J Geophys Res-Atmos* 109(D10): doi:10.1029/2003jd004442
- Huang CM, Zhang SD, Yi F (2005) A numerical study on nonlinear propagation and short-term variability of the migrating diurnal and semidiurnal tides. *Chin Sci Bull* 50(17):1940–1948, doi:10.1360/982004-687
- Huang FT, Mayr HG, Reber CA, Russell J, Mlynczak M, Mengel J (2006) Zonal-mean temperature variations inferred from SABER measurements on TIMED compared with UARS observations. *J Geophys Res* 111(A10): doi:10.1029/2005ja011427
- Huang CM, Zhang SD, Yi F (2007) A numerical study of the impact of nonlinearity on the amplitude of the migrating diurnal tide. *J Atmos Sol-Terr Phys* 69(6):631–648, doi:10.1016/j.jastp.2006.10.008
- Huang CM, Zhang SD, Zhou QH, Yi F, Huang KM (2012) Atmospheric waves and their interactions in the thermospheric neutral wind as observed by the Aricibo incoherent scatter radar. *J Geophys Res-Atmos* 117: doi:10.1029/2012jd018241
- Huang CM, Zhang SD, Yi F, Huang KM, Zhang YH, Gan Q, Gong Y (2013a) Frequency variations of gravity waves interacting with a time-varying tide. *Ann Geophys-Germany* 31(10):1731–1743, doi:10.5194/angeo-31-1731-2013
- Huang KM, Liu AZ, Lu X, Li Z, Gan Q, Gong Y, Huang CM, Yi F, Zhang SD (2013b) Nonlinear coupling between quasi 2 day wave and tides based on meteor radar observations at Maui. *J Geophys Res Atmos* 118: doi:10.1002/jgrd.50872
- Jiang G, Wang W, Xu J, Yue J, Burns AG, Lei J, Mlynczak MG, Russell JM III (2014) Responses of the lower thermospheric temperature to the 9 day and 13.5 day oscillations of recurrent geomagnetic activity. *J Geophys Res Space Phys* 119.
- Khariin VV, Scinocca JF (2012) The impact of model fidelity on seasonal predictive skill. *Geophys Res Lett* 39, L18803, doi:10.1029/2012GL052815
- Khattatov BV, Geller MA, Yudin VA, Hays PB, Skinner WR, Burrage MD, Franke SJ, Fritts DC, Isler JR, Manson AH, Meek CE, McMurray R, Singer W, Hoffmann P, Vincent RA (1996) Dynamics of the mesosphere and lower thermosphere as seen by MF radars and by the high-resolution Doppler imager UARS. *J Geophys Res-Atmos* 101(D6):10393–10404, doi:10.1029/95jd01704
- Lieberman RS (1991) Nonmigrating Diurnal Tides in the Equatorial Middle Atmosphere. *J Atmos Sci* 48(8):1112–1123, doi:10.1175/1520-0469(1991)048<1112:Ndtite>2.0.Co;2
- Lieberman RS, Ortland DA, Yarosh ES (2003) Climatology and interannual variability of diurnal water vapor heating. *J Geophys Res-Atmos* 108(D3): doi:10.1029/2002jd002308
- Lieberman RS, Oberheide J, Hagan ME, Remsberg EE, Gordley LL (2004) Variability of diurnal tides and planetary waves during November 1978-May 1979. *J Atmos Sol-Terr Phys* 66(6–9):517–528, doi:10.1016/j.jastp.2004.01.006
- Lieberman RS, Riggan DM, Ortland DA, Nesbitt SW, Vincent RA (2007) Variability of mesospheric diurnal tides and tropospheric diurnal heating during 1997–1998. *J Geophys Res-Atmos* 112(D20): doi:10.1029/2007jd008578
- Lieberman RS, Ortland DA, Riggan DM, Wu Q, Jacobi C (2010) Momentum budget of the migrating diurnal tide in the mesosphere and lower thermosphere. *J Geophys Res-Atmos* 115: doi:10.1029/2009jd013684
- Lu X, Liu HL, Liu AZ, Yue J, McInerney JM, Li Z (2012) Momentum budget of the migrating diurnal tide in the Whole Atmosphere Community Climate Model at vernal equinox. *J Geophys Res-Atmos* 117: doi:10.1029/2011jd017089
- Manson AH, Luo Y, Meek C (2002) Global distributions of diurnal and semi-diurnal tides: observations from HRDI-UARS of the MLT region. *Ann Geophys-Germany* 20(11):1877–1890
- Manson AH, Meek C, Hagan M, Zhang X, Luo Y (2004) Global distributions of diurnal and semidiurnal tides: observations from HRDI-UARS of the MLT region and comparisons with GSWM-02 (migrating, nonmigrating components). *Ann Geophys-Germany* 22(5):1529–1548
- Marsh DR (2011) Chemical-Dynamical Coupling in the Mesosphere and Lower Thermosphere. In: *Aeronomy of the Earth's Atmosphere and Ionosphere, Vol 2. IAGA Special Sopron Book Springer, Dordrecht*
- Marsh DR, Russell JM (2000) A tidal explanation for the sunrise/sunset anomaly in HALOE low-latitude nitric oxide observations. *Geophys Res Lett* 27(19):3197–3200, doi:10.1029/2000gl000070
- Mayr HG, Mengel JG (2005) Interannual variations of the diurnal tide in the mesosphere generated by the quasi-biennial oscillation. *J Geophys Res-Atmos* 110(D10): doi:10.1029/2004jd005055
- Mayr HG, Mengel JG, Talaat ER, Porter HS, Chan KL (2005) Mesospheric non-migrating tides generated with planetary waves: I. Characteristics *J Atmos Sol-Terr Phys* 67(11):959–980, doi:10.1016/j.jastp.2005.03.002
- McLandress C (1997) Seasonal variability of the diurnal tide: Results from the Canadian middle atmosphere general circulation model. *J Geophys Res-Atmos* 102(D25):29747–29764, doi:10.1029/97jd02645
- McLandress C (1998) On the importance of gravity waves in the middle atmosphere and their parameterization in general circulation models. *J Atmos Sol-Terr Phys* 60(14):1357–1383, doi:10.1016/S1364-6826(98)00061-3
- McLandress C (2002a) The seasonal variation of the propagating diurnal tide in the mesosphere and lower thermosphere. Part I: The role of gravity waves and planetary waves. *J Atmos Sci* 59(5):893–906, doi:10.1175/1520-0469(2002)059<0893: Tsvotp>2.0.Co;2
- McLandress C (2002b) The seasonal variation of the propagating diurnal tide in the mesosphere and lower thermosphere. Part II: The role of tidal heating and zonal mean winds. *J Atmos Sci* 59(5):907–922, doi:10.1175/1520-0469(2002)059<0907: Tsvotp>2.0.Co;2
- McLandress C, Ward WE (1994) Tidal Gravity-Wave Interactions and Their Influence on the Large-Scale Dynamics of the Middle Atmosphere - Model Results. *J Geophys Res-Atmos* 99(D4):8139–8155, doi:10.1029/94jd00486

- McLandress C, Shepherd GG, Solheim BH (1996) Satellite observations of thermospheric tides: Results from the wind imaging interferometer on UARS. *J Geophys Res-Atmos* 101(D2):4093–4114, doi:10.1029/95jd03359
- McLandress C, Ward WE, Fomichev VI, Semeniuk K, Beagley SR, McFarlane NA, Shepherd TG (2006) Large-scale dynamics of the mesosphere and lower thermosphere: An analysis using the extended Canadian Middle Atmosphere Model. *J Geophys Res-Atmos* 111(D17): doi:10.1029/2005jd006776
- McLandress C, Scinocca JF, Shepherd TG, Reader MC, Manney GL (2013) Dynamical Control of the Mesosphere by Orographic and Nonorographic Gravity Wave Drag during the Extended Northern Winters of 2006 and 2009. *J Atmos Sci* 70(7):2152–2169, doi:10.1175/Jas-D-12-0297.1
- Mertens CJ, Schmidlin FJ, Goldberg RA, Remsberg EE, Pesnell WD, Russell JM, Mlyneczek MG, Lopez-Puertas M, Wintersteiner PP, Picard RH, Winick JR, Gordley LL (2004) SABER observations of mesospheric temperatures and comparisons with falling sphere measurements taken during the 2002 summer MacWAVE campaign. *Geophys Res Lett* 31(3): doi:10.1029/2003gl018605
- Miyahara S, Miyoshi Y (1997) Migrating and non-migrating atmospheric tides simulated by a middle atmosphere general circulation model. *Coupling and Energetics in the Stratosphere-Mesosphere-Thermosphere-Ionosphere System* 20(6):1201–1207, doi:10.1016/S0273-1177(97)00773-4
- Miyahara S, Yoshida Y, Miyoshi Y (1993) Dynamic Coupling between the Lower and Upper-Atmosphere by Tides and Gravity-Waves. *J Atmos Terr Phys* 55(7):1039–1053, doi:10.1016/0021-9169(93)90096-H
- Miyahara S, Miyoshi Y, Yamashita K (1999) Variations of migrating and non-migrating tides simulated by the Middle Atmosphere Circulation Model at Kyushu University. *Ionospheric/Thermospheric/Mesospheric Coupling* 24(11):1549–1558, doi:10.1016/S0273-1177(99)00879-0
- Mukhtarov P, Pancheva D, Andonov B (2009) Global structure and seasonal and interannual variability of the migrating diurnal tide seen in the SABER/TIMED temperatures between 20 and 120 km. *J Geophys Res* 114: doi:10.1029/2008ja013759
- Oberheide J, Gusev OA (2002) Observation of migrating and nonmigrating diurnal tides in the equatorial lower thermosphere. *Geophys Res Lett* 29(24): doi:10.1029/2002gl016213
- Oberheide J, Wu Q, Killeen TL, Hagan ME, Roble RG (2006) Diurnal nonmigrating tides from TIMED Doppler Interferometer wind data: Monthly climatologies and seasonal variations. *J Geophys Res* 111(A10): doi:10.1029/2005ja011491
- Oberheide J, Forbes JM, Hausler K, Wu Q, Bruinsma SL (2009) Tropospheric tides from 80 to 400 km: Propagation, interannual variability, and solar cycle effects. *J Geophys Res-Atmos* 114: doi:10.1029/2009jd012388
- Ogibalov VP, Fomichev VI (2003) Parameterization of solar heating by the near IR CO₂ bands in the mesosphere. *Middle Atmosphere Structure and Dynamics* 32(5):759–764, doi:10.1016/S0273-1177(03)00419-8
- Pancheva D, Mukhtarov P, Andonov B (2009) Global structure, seasonal and interannual variability of the migrating semidiurnal tide seen in the SABER/TIMED temperatures (2002–2007). *Ann Geophys-Germany* 27(2):687–703
- Pedatella NM, Liu HL (2012) Tidal variability in the mesosphere and lower thermosphere due to the El Niño-Southern Oscillation. *Geophys Res Lett* 39: doi:10.1029/2012gl053383
- Pedatella NM, Liu HL (2013) Influence of the El Niño Southern Oscillation on the middle and upper atmosphere. *J Geophys Res* 118(5):2744–2755, doi:10.1002/Jgra.50286
- Pirscher B, Foelsche U, Borsche M, Kirchengast G, Kuo YH (2010) Analysis of migrating diurnal tides detected in FORMOSAT-3/COSMIC temperature data. *J Geophys Res-Atmos* 115: doi:10.1029/2009jd013008
- Preusse P, Eckermann SD, Oberheide J, Hagan ME, Offermann D (2001) Modulation of gravity waves by tides as seen in CRISTA temperatures. *Adv Space Res* 27(10):1773–1778, doi:10.1016/S0273-1177(01)00336-2
- Remsberg EE, Marshall BT, Garcia-Comas M, Krueger D, Lingenfelter GS, Martin-Torres J, Mlyneczek MG, Russell JM, Smith AK, Zhao Y, Brown C, Gordley LL, Lopez-Gonzalez MJ, Lopez-Puertas M, She CY, Taylor MJ, Thompson RE (2008) Assessment of the quality of the Version 1.07 temperature-versus-pressure profiles of the middle atmosphere from TIMED/SABER. *J Geophys Res-Atmos* 113(D17): doi:10.1029/2008jd010013
- Sakazaki T, Fujiwara M, Zhang X, Hagan ME, Forbes JM (2012) Diurnal tides from the troposphere to the lower mesosphere as deduced from TIMED/SABER satellite data and six global reanalysis data sets. *J Geophys Res-Atmos* 117: doi:10.1029/2011jd017117
- Scinocca JF, McFarlane NA (2004) The variability of modeled tropical precipitation. *J Atmos Sci* 61(16):1993–2015, doi:10.1175/1520-0469(2004)061<1993:Tvontmp>2.0.Co;2
- She CY, Li T, Collins RL, Yuan T, Williams BP, Kawahara TD, Vance JD, Acott P, Krueger DA, Liu HL, Hagan ME (2004) Tidal perturbations and variability in the mesopause region over Fort Collins, CO (41 N, 105 W): Continuous multi-day temperature and wind lidar observations. *Geophys Res Lett* 31(24): doi:10.1029/2004gl021165
- Shepherd TG (2000) The middle atmosphere. *J Atmos Solar-Terrestrial Phys* 62:1587–1601
- Smith AK (2012) Global Dynamics of the MLT. *Surv Geophys* 33(6):1177–1230, doi:10.1007/s10712-012-9196-9
- Smith AK, Marsh DR, Szymczak AC (2003) Interaction of chemical heating and the diurnal tide in the mesosphere. *J Geophys Res-Atmos* 108(D5): doi:10.1029/2002jd002664
- Smith AK, Garcia RR, Marsh DR, Richter JH (2011) WACCM simulations of the mean circulation and trace species transport in the winter mesosphere. *J Geophys Res* 116, D20115, doi:10.1029/2011JD016083
- Talaat ER, Lieberman RS (1999) Nonmigrating diurnal tides in mesospheric and lower-thermospheric winds and temperatures. *J Atmos Sci* 56(24):4073–4087, doi:10.1175/1520-0469(1999)056<4073:Ndtima>2.0.Co;2
- Teitelbaum H, Vial F (1991) On Tidal Variability Induced by Nonlinear-Interaction with Planetary-Waves. *J Geophys Res* 96(A8):14169–14178, doi:10.1029/91ja01019
- Vial F, Lott F, Teitelbaum H (1994) A Possible Signal of the El-Niño-Southern Oscillation in Time-Series of the Diurnal Tide. *Geophys Res Lett* 21(15):1603–1606, doi:10.1029/94gl01016
- Vincent RA, Tsuda T, Kato S (1988) A Comparative-Study of Mesospheric Solar Tides Observed at Adelaide and Kyoto. *J Geophys Res-Atmos* 93(D1):699–708, doi:10.1029/Jd093id01p00699
- Vincent RA, Kovalam S, Fritts DC, Isler JR (1998) Long-term MF radar observations of solar tides in the low-latitude mesosphere: Interannual variability and comparisons with the GSWM. *J Geophys Res-Atmos* 103(D8):8667–8683, doi:10.1029/98jd00482
- Ward WE (1998) Tidal mechanisms of dynamical influence on oxygen recombination airglow in the mesosphere and lower thermosphere. *Atmospheric Tidal Dynamics and E- and D-Region Physics* 21(6):795–805, doi:10.1016/S0273-1177(97)00676-5
- Ward WE, Oberheide J, Riese M, Preusse P, Offermann D (1999) Tidal signatures in temperature data from CRISTA 1 mission. *J Geophys Res-Atmos* 104 (D13):16391–16403, doi:10.1029/1998jd010019
- Ward WE, Fomichev VI, Beagley S (2005) Nonmigrating tides in equinox temperature fields from the Extended Canadian Middle Atmosphere Model (CMAM). *Geophys Res Lett* 32(3): doi:10.1029/2004gl021466
- Ward WE, Oberheide J, Goncharenko LP, Nakamura T, Hoffmann P, Singer W, Chang LC, Du J, Wang DY, Batista P, Clemesha B, Manson AH, Riggin DM, She CY, Tsuda T, Yuan T (2010) On the consistency of model, ground-based, and satellite observations of tidal signatures: Initial results from the CAWSES tidal campaigns. *J Geophys Res-Atmos* 115: doi:10.1029/2009jd012593
- Warner K, Oberheide J (2014) Nonmigrating tidal heating and MLT tidal wind variability due to the El Niño-Southern Oscillation. *J Geophys Res Atmos* 119:1249–1265, doi:10.1002/2013JD020407
- Wu Q, Killeen TL, Ortland DA, Solomon SC, Gablehouse RD, Johnson RM, Skinner WR, Niciejewski RJ, Franke SJ (2006) TIMED Doppler interferometer (TIDI) observations of migrating diurnal and semidiurnal tides. *J Atmos Sol-Terr Phys* 68(3–5):408–417, doi:10.1016/j.jastp.2005.02.031
- Wu Q, Ortland DA, Killeen TL, Roble RG, Hagan ME, Liu HL, Solomon SC, Xu JY, Skinner WR, Niciejewski RJ (2008a) Global distribution and interannual variations of mesospheric and lower thermospheric neutral wind diurnal tide: 1. Migrating tide. *J Geophys Res* 113(A5):
- Wu Q, Ortland DA, Killeen TL, Roble RG, Hagan ME, Liu HL, Solomon SC, Xu JY, Skinner WR, Niciejewski RJ (2008b) Global distribution and interannual variations of mesospheric and lower thermospheric neutral wind diurnal tide: 2. Nonmigrating tide. *J Geophys Res* 113(A5): doi:10.1029/2007ja012543
- Wu Q, Ortland DA, Solomon SC, Skinner WR, Niciejewski RJ (2011) Global distribution, seasonal, and inter-annual variations of mesospheric semidiurnal tide observed by TIMED TIDI. *J Atmos Sol-Terr Phys* 73(17–18):2482–2502, doi:10.1016/j.jastp.2011.08.007
- Xie F, Wu DL, Ao CO, Mannucci AJ (2010) Atmospheric diurnal variations observed with GPS radio occultation soundings. *Atmos Chem Phys* 10 (14):6889–6899, doi:10.5194/acp-10-6889-2010

- Xu JY, Liu HL, Yuan W, Smith AK, Roble RG, Mertens CJ, Russell JM, Mlynczak MG (2007a) Mesopause structure from thermosphere, ionosphere, mesosphere, energetics, and dynamics (TIMED)/sounding of the atmosphere using broadband emission radiometry (SABER) observations. *J Geophys Res-Atmos* 112(D9): doi:10.1029/2006jd007711
- Xu JY, Smith AK, Yuan W, Liu HL, Wu Q, Mlynczak MG, Russell JM (2007b) Global structure and long-term variations of zonal mean temperature observed by TIMED/SABER. *J Geophys Res-Atmos* 112(D24): doi:10.1029/2007jd008546
- Xu JY, Smith AK, Liu HL, Yuan W, Wu Q, Jiang GY, Mlynczak MG, Russell JM (2009a) Estimation of the equivalent Rayleigh friction in mesosphere/lower thermosphere region from the migrating diurnal tides observed by TIMED. *J Geophys Res-Atmos* 114: doi:10.1029/2009jd012209
- Xu JY, Smith AK, Liu HL, Yuan W, Wu Q, Jiang GY, Mlynczak MG, Russell JM, Franke SJ (2009b) Seasonal and quasi-biennial variations in the migrating diurnal tide observed by Thermosphere, Ionosphere, Mesosphere, Energetics and Dynamics (TIMED). *J Geophys Res-Atmos* 114: doi:10.1029/2008jd011298
- Xu JY, Smith AK, Jiang GY, Yuan W (2010) Seasonal variation of the Hough modes of the diurnal component of ozone heating evaluated from Aura Microwave Limb Sounder observations. *J Geophys Res-Atmos* 115: doi:10.1029/2009jd013179
- Xu JY, Smith AK, Liu M, Liu X, Gao H, Jiang GY, Yuan W (2014) Evidence for non-migrating tides produced by the interaction between tides and stationary planetary waves in the stratosphere and lower mesosphere. *J Geophys Res-Atmos* 119: doi:10.1002/2013JD020150
- Yi F (2001) Short-term variability and temporary structures of tides and mean wind in the polar summer mesosphere. *J Atmos Sol-Terr Phys* 63(8):749–757, doi:10.1016/S1364-6826(01)00005-0
- Yuan T, She CY, Hagan ME, Williams BP, Li T, Arnold K, Kawahara TD, Acott PE, Vance JD, Krueger D, Roble RG (2006) Seasonal variation of diurnal perturbations in mesopause region temperature, zonal, and meridional winds above Fort Collins, Colorado (40.6 degrees N, 105 degrees W). *J Geophys Res-Atmos* 111(D6): doi:10.1029/2004jd005486
- Yuan T, She CY, Krueger DA, Sassi F, Garcia R, Roble RG, Liu HL, Schmidt H (2008) Climatology of mesopause region temperature, zonal wind, and meridional wind over Fort Collins, Colorado (41 degrees N, 105 degrees W), and comparison with model simulations. *J Geophys Res-Atmos* 113(D3): doi:10.1029/2007jd008697
- Yue J, Xu J, Chang LC, Wu Q, Liu H-L, Lu X, Russell J III (2013) Global structure and seasonal variability of the migrating terdiurnal tide in the mesosphere and lower thermosphere. *J Atmos Sol Terr Phys* 105–106:191–198, doi:10.1016/j.jastp.2013.10.010
- Zeng Z, Randel W, Sokolovskiy S, Deser C, Kuo YH, Hagan M, Du J, Ward W (2008) Detection of migrating diurnal tide in the tropical upper troposphere and lower stratosphere using the Challenging Minisatellite Payload radio occultation data. *J Geophys Res-Atmos* 113(D3): doi:10.1029/2007jd008725
- Zhang SP, Roble RG, Shepherd GG (2001) Tidal influence on the oxygen and hydroxyl nightglows: Wind Imaging Interferometer observations and thermosphere/ionosphere/mesosphere electrodynamic general circulation model. *J Geophys Res* 106(A10):21381–21393, doi:10.1029/2000ja000363
- Zhang SD, Yi F, Hu X (2004) MF radar observation of mean wind and tides of winter mesopause (80–98 km) region over Wuhan (30 degrees N, 114 degrees E). *J Atmos Sol-Terr Phys* 66(1):15–25, doi:10.1016/j.jastp.2003.10.006
- Zhang XL, Forbes JM, Hagan ME, Russell JM, Palo SE, Mertens CJ, Mlynczak MG (2006) Monthly tidal temperatures 20–120 km from TIMED/SABER. *J Geophys Res* 111(A10): doi:10.1029/2005ja011504

doi:10.1186/1880-5981-66-103

Cite this article as: Gan *et al.*: Climatology of the diurnal tides from eCMAM30 (1979 to 2010) and its comparison with SABER. *Earth, Planets and Space* 2014 **66**:103.

Submit your manuscript to a SpringerOpen[®] journal and benefit from:

- Convenient online submission
- Rigorous peer review
- Immediate publication on acceptance
- Open access: articles freely available online
- High visibility within the field
- Retaining the copyright to your article

Submit your next manuscript at ► springeropen.com